

**DEVELOPMENT OF ITO
(In₂O₃ – SnO₂) BASED GAS SENSORS**

Sadna IŞIK

**Master's Thesis
Department of Nanoscience and Nanoengineering,
Nanomaterials Program
Assoc. Prof. Dr. Emre GÜR
2015
All rights reserved**

**ATATÜRK UNIVERSITY
GRADUATE SCHOOL OF NATURAL AND APPLIED SCIENCES**

MASTER'S THESIS

DEVELOPMENT OF ITO ($\text{In}_2\text{O}_3 - \text{SnO}_2$) BASED GAS SENSORS

Sadna IŞIK

**DEPARTMENT OF NANOSCIENCE AND NANOENGINEERING
Nanomaterials Program**

**ERZURUM
2015**

All rights reserved



TURKISH REPUBLIC
ATATURK UNIVERSITY
GRADUTE SCHOOL of NATURAL and APPLIED
SCIENCES



THESIS APPROVAL FORM

DEVELOPMENT OF ITO ($\text{In}_2\text{O}_3 - \text{SnO}_2$) BASED GAS SENSORS

This study, prepared by Sadna IŞIK, under supervision of Assoc. Prof. Emre GÜR, has been approved on the date of 13/ 01/ 2015 as Master Thesis, in the Department of Nanoscience and Nanoengineering – Graduate School of Natural and Applied Sciences, by the below-named thesis committee with **majority/unanimously** (..../....).

President : Prof. Mehmet BİBER

Member : Assoc. Prof. Emre GÜR

Member : Assoc. Prof. Önder METİN

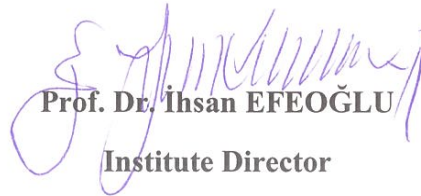
Signature :

Signature :

Signature :

The above-mentioned result;

Has been approved in accordance with Institute Administrative Committee on the date of 29. / 01. / 2015 and resolution number 04. / 123...


Prof. Dr. İhsan EFEOĞLU
Institute Director

Note: Reproduction of authentic or quoted notifications, charts, figures and images of this thesis is subject to provisions of Law on Intellectual and Artistic Works law number 5846.

ÖZET

Yüksek Lisans Tezi

İTO ($\text{In}_2\text{O}_3 - \text{SnO}_2$) TABANLI GAZ SENSÖR GELİŞTİRİLMESİ

Sadna IŞIK

Atatürk Üniversitesi
Fen Bilimleri Enstitüsü
Nanobilim ve Nanomühendislik Anabilim Dalı
Nanomalzeme Bilim Dalı

Danışman: Doç. Dr. Emre GÜR

Metal oksit geniş bant aralıklı aygıtlar, yeni nesil gaz sensörleri için gelecek vadetmektedir. Bu tez, indirgeyici hidrojeni (H_2) ve yükseltgeyici karbon dioksiti (CO_2) algılayan, direnç tabanlı geniş bant aralıklı yarı iletken gaz algılama aygıtları üzerine gerçekleştirilmiştir. RF magnetron saçırma sistemi ile şeffaf indiyum kalay oksit ince film tabakaları büyütülmüştür. İnce filmler Al arka kontak üzerine büyütülmüş ve ince film yüzeyi gaz algılama için açık bırakılmıştır. Bu çalışmada, H_2 ve CO_2 gazları için duyarlılık gösteren üç farklı İTO gaz sensörü incelenmiştir. Ayrıca, yapısal, morfolojik ve optik özelliklerine bağlı olarak duyarlılığın nasıl değiştiği de araştırılmıştır. X-ışını difraksiyon ölçümleri, SEM görüntüleri, soğurma ölçümleri ve gaz sensörü ölçümleri ile O_2 kısmi basıncına bağlı olarak aygıtların kristal yönelim, tane boyutu, bant aralığı, başarımlı ölçüsü ve gaz sensörü duyarlılığı özelliklerinin değişimi gösterilmiştir. Tüm hazırlanan filmlerde %90'ın üzerinde geçirgenlik değerleri bulunmuş ve temel soğurma kenarında kayma ile birlikte ve direk optik yasak enerji aralığı 3,46 ve 4,13 eV arasında olduğu bulunmuştur. Soğurma ölçümleri, O_2 kısmi basıncının artması ile yasak enerji bant aralığının ve başarımlı ölçüsünün arttığını göstermiştir. XRD verilerine göre (400) ve (411) düzlemlerine ait piklerin baskın olduğu ve bu piklerin şiddetlerinin ve oranlarının O_2 kısmi basıncına göre değiştiği gösterilmiştir. Bu aygıtlar, 50°C sıcaklığın üzerinde ve 400 sccm konsantrasyonlarında H_2 ve CO_2 için duyarlıdır. Gaz algılama performansı, farklı ölçüm sıcaklıklarında (30°C ile 200°C aralığında), dinamik gaz algılama sistemi kullanılarak gerçekleştirilmiştir. Aygıtların 200°C sıcaklıkta maksimum H_2 duyarlılığı (RS =%22) gösterdiği tespit edilmiştir. Ayrıca aygıtlar, kısa cevap zamanı (92,3 s) ve kısa geri dönme zamanı (24,2 s) göstermişlerdir.

2015, 87 Sayfa

Anahtar Kelimeler: Gas sensör, İTO, RF magnetron saçırma sistemi, Başarımlı ölçüsü.

ABSTRACT

Master Thesis

DEVELOPMENT OF ITO ($\text{In}_2\text{O}_3 - \text{SnO}_2$) BASED GAS SENSORS

Sadna IŞIK

Atatürk University
Graduate School of Natural and Applied Sciences
Department of Nano science and Nano Engineering
Department of Nanomaterial

Supervisor: Assoc. Prof. Dr. Emre GÜR

Wide bandgap metal oxide based devices are promising candidates for the next generation gas sensors. In this thesis, resistive based wide band gap semiconductor gas sensing devices detecting reducing-hydrogen (H_2) and oxidizing-carbon dioxide (CO_2) are presented. Transparent Indium tin oxide (ITO) thin film layers were deposited employing RF magnetron sputtering system. The thin films are back contacted with Al leaving thin film surface free for gas detection. In this work three different types of ITO gas sensors were investigated for their sensitivity for H_2 and CO_2 gases. Also discussed how sensitivity varies according to structural, morphological, optical properties and O_2 partial pressure. The X-ray diffraction measurements, SEM images absorption measurements and gas sensing measurements have revealed that the crystal orientation, growth rate, band gap, figure of merit and gas sensor sensitivity changed relevant to O_2 partial pressure introduced to thin film. All the prepared films show the larger values of transmittance $>90\%$ along with the shift in the fundamental absorption edge and the direct optical band gap which was found to be between 3.46 and 4.13 eV. Absorption measurements show bandgap and figure of merit increasing with increase of O_2 partial pressure. XRD data reveals the dominant peaks as (400) and (441) also while O_2 partial pressure has effects on the intensities and the ratios of these peaks. These devices are sensitive to H_2 and CO_2 concentrations well below 400 sccm at over 50°C temperature. Gas-sensing performance was conducted using dynamic gas-sensing system, at elevated temperatures in the range of 30°C to 200°C . The maximum sensitivity ($R_S=22\%$) to H_2 was found at the temperature of 200°C . CO_2 results show dependency of the temperature. Response time (92.3 s) and recovery times (24.2 s) are the main features of this device.

2015, 87 pages

Keywords: Gas sensor, ITO, RF magnetron sputtering system, Figure of Merit.

ACKNOWLEDGMENT

My deepest appreciation to my advisor Associate Professor Dr. Emre GÜR for giving me unequal support, encouragement, intellectual input and friendship with bona fides in every single days throughout the past two years. His modesty and humility nature inspired to create great environment to be successful and without his role this would not be feasible, I truly admire his exceptional support, guidance that forced me to confer on quality outcome.

A big thank to Professor Cyrus SHAFAI for accepting and hosting me as a visiting research student at University of Manitoba. I am very grateful to him for his patience and making me accessible to all kind of resource, so everything went successfully.

I wish to thank to my colleagues Miss. Zineb BENZAIT, Mr. Ömer ÇOBAN and Miss. Ceydanur ÖZTÜRK for their help, good humor as well as providing friendly and inspiring environment for conducting research and studies.

I am especially grateful to Ms. Amy DARIO, Mr. Dwayne CHRUSCH, Mr. Tao CHEN, Miss. Meiting LI, Mr. Byoung Youl PARK, Mr. ZHOU, University of Manitoba for their assistance and friendship during my visit to University of Manitoba.

My heartfelt gratitude and respect to Prof. Ümit İNCEKARA, Atatürk University.

My special thanks to Mr. Haleem NAUSHATH, Mr. Garry BISTYAK University of Manitoba for recommending me to Prof Cyrus SHAFAI.

My thanks extended to the academic and administrative staff of the Institute of Natural and applied Sciences, Department of Solid state Physics, Department of Nanoscience & Nanoengineering of Atatürk University and Nano Laboratory of Erzincan University for providing resources and helping to solve the obstacles I faced during my researches.

I am very grateful to my loving husband Associate Professor Dr. Memet IŞIK, Atatürk University for taking care and giving hands to fulfill my dreams from the day I reborn in Turkey.

Sadna IŞIK

January, 2015

CONTENTS

ÖZET.....	i
ABSTRACT.....	ii
ACKNOWLEDGMENT.....	iii
SYMBOLS and ABBREVIATIONS OF CONTENT.....	vi
INDEX OF FIGURES.....	viii
INDEX OF CHARTS.....	xi
1. INTRODUCTION.....	1
1.1. Semiconductor Gas Sensors (SGS).....	5
1.2. Thesis Organization.....	11
2. THEORETICAL FUNDAMENTALS.....	14
2.1. Gas Sensor.....	14
2.2. Sputtering Technique.....	17
2.3. Indium Tin Oxide.....	20
2.4. Resistivity and Sheet Resistant.....	24
2.5. Two-Point vs Four-Point Probe.....	25
2.6. Metal - Semiconductor Ohmic Contacts.....	27
2.7. Absorption.....	29
2.7.1. Quantities for semiconductor spectroscopy (Reflectance, Transmittance and absorbance).....	30
2.7.2. UV-Vis-NIR Spectrophotometry and band gap analysis.....	31
2.7.3. Energy band gap (E_g).....	32
2.8. Determining the Structure of ITO Films by X-ray Diffraction.....	33
2.9. Scanning Electron Microscopy (SEM).....	33
2.10. Etching.....	34
3. MATERIALS and METHODOLOGIES.....	37
3.1. Cleanroom.....	37
3.2. RF/DC Magnetron Sputtering System.....	38
3.3. Substrate Cleaning.....	39
3.4. ITO Thin film Deposition.....	40

3.4.1. Al Deposition for Metal Electrode of the Gas Sensor.....	43
3.5. Photo Lithography	45
3.6. Gas Chamber	52
4. EXPERIMENTAL RESULTS and DISCUSSION	56
4.1. Characterization of ITO Thin films (XRD, SEM, EDAX and Absorption Techniques)	56
4.2. Gas Sensor characterization and measurements.....	69
5. CONCLUSION.....	79
5.1. Outlook and Future Work.....	83
REFERENCES	84
RESUME	88

SYMBOLS and ABBREVIATIONS OF CONTENT

Symbols

Å	Angstrom
°C	Centigrade Degree
cm ⁻³	Centimeter cubic
nm	Nano metre
%	Percentage

Abbreviations

2DEG	Two dimensional electron gas
2θ	Diffraction angle
CMOS	Complementary metal–oxide–semiconductor
CVD	Chemical vapor deposition
DC/dc	Direct current
DI	De-ironized
DUT	Device under test
E	Direct transition energy
eV	Electron volt
FOM	Figure of Merit
HEMTs	High electron mobility transistors,
h ν	Photon energy
IPA	Iso propanol
MFC	Mass flow controller
MOS	Metal–oxide–semiconductor
n _e	Density
P	Pressure
ppm	Parts per million

PR	Photo resist
PVD	Plasma vapor deposition
QMB	Quartz crystal microbalances
RF/rf	Radio frequency
Rpm	Rotation per minute
S	Sensitivity
SAW	Surface acoustic wave
SE	Selectivity
SEM	Scanning Electron Microscopy
SR	Sheet Resistance
T	Heat of temperature
T	Torr
T _{Opt}	Optimum detection
UV	Ultra violet
UV-Vis-NIR	Ultraviolet-visible-near infrared
W	Watt
XRD	X-ray diffraction
α	Absorption coefficient
μ	Carrier mobility,
ρ_e	Resistivity
σ	Electrical conductivity
T _{rec}	Recovery time
T _{res}	Response time
ϕ	Function
Φ_s	Work function
χ_e	Electron affinity

INDEX OF FIGURES

Figure 1.1. Current–voltage (I–V) curves for electrical breakdown	2
Figure 1.2. Canary in a cage and Davey’s Lamp	4
Figure 1.3. Change in resistance of GaN nanowires, either with or without Pd coatings, as a function of gas ambient switched in and out of the test chamber	8
Figure 2.1. Schematic of a resistance based SMO hydrogen sensor.....	14
Figure 2.2. Gas sensing mechanism	16
Figure 2.3. Schematic illustrations of the (a) convention dc-diode and (b) planar magnetron cathode sputtering	19
Figure 2.4. Two non-equivalent sites of In atoms in In_2O_3 crystal	21
Figure 2.5. Assumed parabolic band structure of undoped In_2O_3 and the effect of Sn doping In ITO films, the fundamental absorption edge shifts towards high energy as the free carrier density increases. The widening of the band gap is known as Burstein- Moss shift (BM).....	24
Figure 2.6. Two-terminal and four-terminal resistance measurement arrangements.....	26
Figure 2.7. Two-point probe arrangement showing the probe resistance R_p , the contact resistance R_c , and the spreading resistance R_{sp}	26
Figure 2.8. Showing incident, reflected and transmitted intensities	31
Figure 2.9. Basic mechanisms in wet chemical etching.....	34
Figure 3.1. Particle-size distribution curve	37
Figure 3.2. How dust particles can interfere with photo mask patterns	38
Figure 3.3. MRC 8667 RF/DC sputtering system.....	38
Figure 3.4. ITO loaded and ready for sputtering.....	41
Figure 3.5. 14 cm 99.99% purity ITO target.....	41
Figure 3.6. The patterned Al glass substrate mounted in the RF sputtering system to deposit ITO thin film using shadow/tensile mask.....	44
Figure 3.7. ITO deposited thin film device (a) cross sectional (b) schematic view under the optical microscope (c) Physical ITO deposited device under microscope	44

Figure 3.8. Simple lithographic process schematic summary.....	46
Figure 3.9. Computer aid photo mask image	47
Figure 3.10. Chrome coated glass physical photo mask	47
Figure 3.11. Mask Aligner	48
Figure 3.12. Photo resisted, UV exposed, developed glass substrate under optical microscope.....	49
Figure 3.13. Apparatus for Al etching	50
Figure 3.14. Preparation for wet (isotropic) etching	51
Figure 3.15. The patterned (etched) glass substrate view under optical microscope.....	52
Figure 3.16. Gas chamber	53
Figure 3.17. Schematic drawing of the gas delivery system.....	53
Figure 3.18. Output of the sample gas sensing measurement dynamically and saved backup data using LabVIEW program.....	55
Figure 4.1. XRD results of the thin films grown at O ₂ partial pressure at a) P(O ₂) = 0 % (pure ITO, Device 5) b) P(O ₂) = 2.7 %	57
Figure 4.2. XRD results of the thin films grown at O ₂ partial pressure at a) P(O ₂) = 13.5 % (Device 4), b) P(O ₂) = 16.3 % (Device 3)	57
Figure 4.3. XRD results of the thin films grown at O ₂ partial pressure at a) P(O ₂) = 11.74 % b) P(O ₂) = 11.74 %	57
Figure 4.4. Shows increase of O ₂ partial pressure decrease the crystallinity of the thin films.....	58
Figure 4.5. a) SEM and EDAX images for P (O ₂) = 0% (pure ITO-Device 5) b) P (O ₂) = 2.7%	59
Figure 4.6. a) P(O ₂) = 13.5 % (Device 4) b) P(O ₂) = 16.3 % (Device 3)	60
Figure 4.7. SEM and EDAX images for P(O ₂) = 11.7 %.....	60
Figure 4.8. Growth rate vs O ₂ partial pressure variation.....	62
Figure 4.9. Resistivity vs O ₂ partial presure variation	62
Figure 4.10. Absorption measurements of the ITO thin films a) 200-1000 nm b) 200-450 nm	63
Figure 4.11 a) Absorption coefficient and b) Square absorption coefficient vs energy graph for pure ITO	64

Figure 4.12. a. Absorption coefficient and b. Square absorption coefficient vs energy graph for (2.7% O ₂).....	65
Figure 4.13. a. Absorption coefficient and b. Square absorption coefficient vs energy graph for (6.9% O ₂).....	65
Figure 4.14. a. Absorption coefficient and b. Square absorption coefficient vs energy graph for (21.3% O ₂).....	66
Figure 4.15. a. Absorption coefficient and b. Square absorption coefficient vs energy graph for (25% O ₂).....	66
Figure 4.16. a. Absorption coefficient and b. Square absorption coefficient vs energy graph for (11.7 % O ₂).....	67
Figure 4.17. Bandgap variation with reference to the O ₂ partial pressure	68
Figure 4.18. The figure shows very high transmittance of the grown ITO films.....	68
Figure 4.19. ITO 3 (16.3% O ₂) Device CO ₂ at 200°C	72
Figure 4.20. ITO3 (16.3% O ₂), a. H ₂ at 30°C, b. H ₂ at 200°C.....	72
Figure 4.21. ITO4 (13.5% O ₂) a. CO ₂ at 30°C, b. CO ₂ at 200°C	74
Figure 4. 22. ITO4 (13.5% O ₂) a. H ₂ at 30°C, b. H ₂ at 200°C.....	74
Figure 4.23. ITO5 a. CO ₂ at 30°C, b. CO ₂ at 50°C	75
Figure 4.24. ITO5 a. CO ₂ at 100°C, b. CO ₂ at 150°C	75
Figure 4.25. ITO5 a CO ₂ 30 °C., b. CO ₂ at 200°C, Temperature vs Responsivity	76
Figure 4.26. ITO5 a. H ₂ at 30°C, b. H ₂ at 200°C	76
Figure 4.27. Changing the resistance on diffefrent Gas Concentration (sccm)	77
Figure 5.1. Responsivity, Response time, Recovery time for ITO 3, 4, 5 Device at 200°C a. CO ₂ b. H ₂	81

INDEX OF CHARTS

Chart 2.1. Gas sensors technologies and its measuring parameters.....	15
Chart 3.1. Growth conditions for ITO thin film	42
Chart 3.2. Summarized conditions and results of ITO growth	42
Chart 3.3. Growth conditions for ITO device	43
Chart 3.4. Prescribed Ar and O ₂ percentages for ITO device.....	43
Chart 3.5. Sputter chamber conditions and desired recipe for the Al thin film	44
Chart 3.6. Etchants for Insulators and Conductors	51
Chart 3.7. Input parameters for measurements	54
Chart 4.1. Summary of the XRD results and calculation	59
Chart 4.2. Summarized chamber conditions and FPP results.	61
Chart 4.3. Bandgap Variation	67
Chart 4.4. Figure of Merit (FOM) of ITO thin films	69
Chart 4.5. Comparison of ITO 3 (16.3% O ₂).....	73
Chart 4.6. Comparison of ITO 4 (13.5% O ₂).....	73
Chart 4.7. Comparison of ITO 5 (0% O ₂).....	75
Chart 4.8. Comparison of ITO 5 (0% O ₂) for CO ₂ Temperature dependency	76

1. INTRODUCTION

Sense is a physiological capacity of organism that provides data for perception. Human also have multitude senses but degree of sensing capability is limited. One of the advantages of sensing is true alarm to hazards. Some hazards coming from directly related to harmful gases. Atmosphere is a mixture of useful and harmful gases i.e. Oxygen and Methane respectively. Additional natural and artificial gases released to atmosphere as a result of increased energy and resource consumption, i.e. mines-methane gas, industry-ammonia gas, automobile-hydrogen gas used as energy alternative, carbon dioxide-global warming. Usual and unusual gas flows to atmosphere should be recognized in advance to avoid disasters. To solve such issues artificial sensing/electronic sensing systems have been developed (Eggins 2004). Formally the mimic of gas sensors idea came from physical sensors eyes, ears, nose and fingers to be as they detect sound, light, smell and heat. Physical sensor nose smells small quantities of chemicals (Eggins 2004). The nose is an extremely sensitive and selective instrument can distinguish different chemical substances qualitatively and can overall idea of 'quantity' down to very low detection limits (Eggins 2004). Nowadays various type of electronic noses/gas sensors available in everywhere. These gas sensors play vital roles in many areas such as automobile, health, safety, aerospace, environmental monitoring (Modi *et al.* 2003).

A sensor is a device that detects/senses a signal, physical condition and chemical compounds or any device that converts a signal from one form to another. Sensors are mostly electrical or electronic. Some few examples are acoustic, sound, vibration i.e. lace sensor - a guitar pickup, automotive, transportation i.e. air-fuel ratio meter, chemical i.e. smoke detector, electric current, electric potential, magnetic, radio i.e. galvanometer, environment, weather, moisture, humidity thermal, heat, temperature i.e. thermometer.

A chemical sensor is a self-contained analytical device that can provide information about the chemical composition of its environment. Gas sensor is a subclass of chemical

sensor that measures the concentration of gas in its vicinity (Anonymous 2014a). Gas sensor interacts with a gas to measure its concentration by adsorption. Each gas has a unique breakdown voltage as shown in Figure 1.1. The concentration of the gas can be determined by measuring the current discharge in the device (Ashish *et al.* 2003).

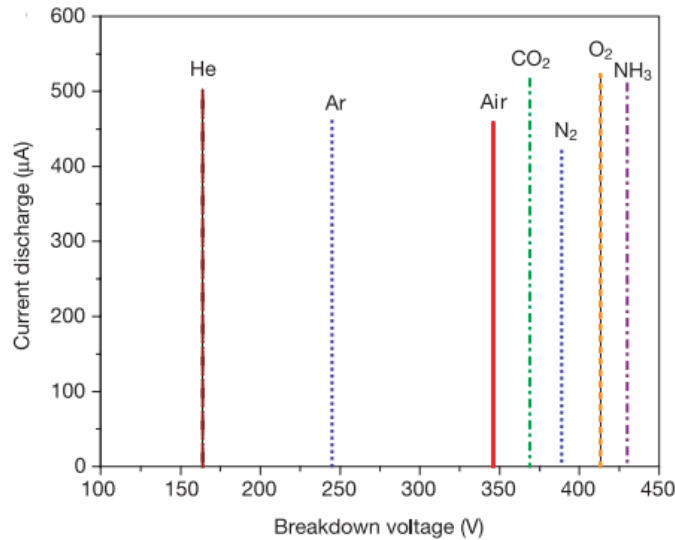


Figure 1.1. Current–voltage (I–V) curves for electrical breakdown

a: I–V curves for NH₃, CO₂, N₂, O₂, He, Ar and air, showing distinct breakdown voltages; ammonia discharges the highest breakdown voltage, and helium the lowest

Gas sensors are used in various end-use industries. There have been numerous developments in gas sensing technology. Gas sensors prove to be highly effective in measuring gas concentrations in the event of a leak. The global gas sensors market was estimated at USD 1,700.5 million in 2012, and is expected to grow at a compound annual growth rate (CAGR) of 5.1% from 2014 to 2020 (Anonymous 2014a). According to a new technical market research report, gas sensors and gas metering: Applications and Markets (IAS012B) from BCC Research, the global market for gas sensors and gas metering is worth an estimated \$3.9 billion in 2010, but is expected to increase to nearly \$5.2 billion in 2015, for a 5-year CAGR of 5.9%. According to a global chemical sensors market survey conducted in 2010, a greater than 17 billion dollar market for chemical sensors is estimated by 2015 (Anonymous 2014a). In another report, the chemical sensor market is expected to grow by up to 6 billion dollars by 2014 in the US with an 8.6% annual growth rate (Anonymous 2014a).

These global market reports predict importance of gas sensors. In addition to being used in hazardous environments, wireless gas sensors can also be installed at lower costs in any field. Therefore research and fabrication smart gas sensors which has considerably widened in application scope. Need for ensuring safety in workplaces and consume of green fuel is expected to be the key driving force for the market in future. Regulations in developed markets of North America and Europe mandate the use of these sensors in potentially hazardous environments. Process and manufacturing industries involve the use of various toxic and combustible gases including hydrogen sulfide and nitrogen dioxide. Continual monitoring the concentration of these gases using sensors supports in averting any possible mishaps (Anonymous 2014a).

Milestone in a gas detection history probably starts by the canary in a cage which is first reported gas monitors. Canaries are much more susceptible than humans to low oxygen, methane gas, or CO gas. People used them to detect poisonous gases in mines because of its highly sensitive nature towards gases. They would stop singing and eventually die in the presence of these gases, signaling the miners to exit the mine quickly. Generally two canaries used for the detection. This was the first kind of gas sensors used in 1920s (Lang 2008). The flame safety lamp called Davey's lamp" Invented by Sir Humphry Davey of England in 1815. With reference to the concentration of the gas the flame height was calibrated present in the ambient flame contained within a glass sleeve and with a flame arrester vise-versa higher flame means methane gas present lower flame means low oxygen.

The idea of using semiconductors as gas sensitive devices 1953 when Brattain and Bardeen first reported gas sensitive effects on Ge who won the joint Nobel prize in Physics (Michael 2013). Later, gas sensing effects of metal oxides was found. In 1968, Taguchi Figaro revolutionized this field by identifying the metal oxide materials as gas sensing elements. Taguchi finally brought semiconductor sensors based on metal oxides to an industrial product called Taguchi-type sensors (Barsan *et al.* 2007). Today, there are many companies offering variety of semiconducting gas sensors, such as Figaro, FIS, MICS, CityTech, Applied Sensor, UST, Microsens and Paragon.



Figure 1.2. Canary in a cage and Davey's Lamp (Lang 2008)

Chemical sensors have gained in importance in the past decade for applications that include homeland security, medical and environmental monitoring, automobile and also food safety. A desirable goal is the ability to simultaneously analyze a wide variety of environmental and biological gases and liquids in the field and to be able to selectively detect a target analytic with high specificity and sensitivity (Pearton *et al.* 2010).

The important parameters and performance of gas sensors are sensitivity, analysis range, selectivity, cross-sensitivity, stability, reliability, accuracy, resolution, linearity, response time, lifetime, calibration frequency, cost, usability and tolerance to environmental conditions. Selectivity of gas sensor should be always greater than one. Selectivity equals to sensitivity of particular molecule divided by sensitivity towards to interferon. There can be many factors influencing sensitivity performance of gas sensors such as surface reactions such as different materials for gas sensor, noble metal additives, high surface areas, porous structure; grain size is useful to enhance the sensitivity, external causes, like temperature and humidity, (Gardon *et al.* 2013). In recent years variety of gas sensors developed by transition-metal oxides including Fe_2O_3 , NiO , Cr_2O_3 , non-transition-metal oxides which include: (a) pre-transition-metal oxides i.e. Al_2O_3 and (b) post-transition-metal oxides i.e. ZnO , SnO_2 . Many metal oxides are suitable for detecting combustible, reducing, or oxidizing gases by conductive measurements. Some oxides show a gas response in their conductivity i.e. In_2O_3 , WO_3 , TiO_2 . Metal oxides selected for gas sensors can be determined from their electronic structure and the properties.

Different types of gas sensors influenced by their properties such as solid-state sensors AlGaIn/GaN - high electron mobility transistors, (HEMTs) show a strong dependence of source/drain current on the piezoelectric polarization. Furthermore, spontaneous and piezoelectric polarization induced surface and interface charges can be used to develop very sensitive but robust sensors for the detection of gases, Pt-gated GaN Schottky diodes and $\text{Sc}_2\text{O}_3/\text{AlGaIn}/\text{GaN}$ metal-oxide semiconductor diodes also show large change in forward currents upon exposure to H_2 containing ambient (Ali 2006). However, nitrides are not as thermodynamically stable in oxygen ambient as the oxide semiconductor but oxide doped with aluminum oxide indium-tin-oxide (90% In_2O_3 and 10% SnO_2) are thermodynamically stable (Yang and Tian 2007).

1.1. Semiconductor Gas Sensors (SGS)

It is necessary to reveal the sensing mechanism of metal oxide gas sensors which is helpful for designing and fabricating novel gas sensing materials with excellent performance. Although the exact fundamental mechanisms that cause a gas response are still controversial, it is essentially responsible for a change in conductivity that trapping of electrons at adsorbed molecules and band bending induced by these charged molecules (Batzill *et al.* 2005).

Among the different useful solid-state sensors, metal oxide gas sensors provide an excellent sensing response in front of a wide range of target gases by means of low cost materials and manufacturing. Being first discovered at the middle of twentieth century, many patents have been developed during the last decades and by now it is a commercialized item by many international companies. In addition, a considerable amount of research is being published in this line due to this technology is broadly interdisciplinary. A well-established market is found at present day and its main applications are combustible gas monitoring, humidity or oxygen sensing. However, several emerging markets are maturing in other fields like air cleaners equipped with an air-quality sensor for being installed in either car cabins or houses and more challenging ones as sensing toxic or hazardous gases (Gardon *et al.* 2013).

Conductometric gas sensors based on semiconducting metal oxides are actually one of the most investigated groups of gas sensors. They have attracted the attention of many users and scientists interested in gas sensing under atmospheric conditions due to its low cost, flexibility associated to their production, simplicity of their use and large number of detectable gases/possible application fields (Barsan *et al.* 2007).

Metal oxides represent many class of materials properties cover entire range from metals to semiconductors and insulators. Almost all of the material science and physics in areas including superconductivity and magnetism metal oxides possess a broad range of electronic, chemical, and physical properties that are often highly sensitive to changes in their chemical environment (Eggins 2004). Many scientists and engineers have studied metal oxide thin films as electronic materials due to their semiconducting behavior, structural simplicity and low cost. In the field of gas/chemical sensing, the electrical conductivity of semiconductors varies with the composition of the gas/chemical atmosphere surrounding them. Semiconductor oxide-based gas sensors are classified according to the direction of the conductance change due to the exposure to reducing gases as “n”-type (conductance increases, i.e. In_2O_3 , ZnO , and SnO_2 or “p”-type (conductance decreases, i.e. Cr_2O_3 and CuO). This classification is related to the (surface) conductivity type of the oxides, which is determined by the nature of the dominant charge carriers at the surface, that is, electrons or holes. The gas-sensing properties strongly depend on the surface an operating temperature of the materials. The surface of these oxides can be modified using various synthesis techniques. Metal oxide gas sensors use an appropriate material, either in bulk form or in thick or thin film form as gas sensing element. However, in recent time, nanostructured thin films are used, since it gives better control on gas sensing properties of a material and large surface to volume ratio (Gong *et al.* 2005).

The gas/semiconductor surface interactions on which is based the gas-sensing mechanism of SGS occur at the grain boundaries of the polycrystalline oxide film. They generally include reduction/oxidation processes of the semiconductor, adsorption of the chemical species directly on the semiconductor and/or adsorption by reaction with

surface states associated with pre-adsorbed ambient oxygen, electronic transfer of delocalized conduction-band electrons to localized surface states and vice versa, catalytic effects and in general complex surface chemical reactions between the different adsorbed chemical species (Nicolae *et al.* 2012). The effect of these surface phenomena is a reversible and significant change in electrical resistance (i.e. a resistance increase or decrease under exposure to oxidizing respectively reducing gases referring as example to an n-type semiconductor oxide). This resistance variation can be easily observed and used to detect chemical species in the ambient. The influence of these surface chemistry phenomena on the sensor response may be understood on the base of the charge-transfer model (CTM) and the modified band model of semiconducting metal oxide sensor devices that take into account also the effects of additives, dopants, grain size as well as contacts. According to this model, the changes in the electrical resistance of the sensor are described by the formation of depletion space-charge layers at the surface and around the grains, with upwards bending of the energy bands. Surface energy barriers for conduction electrons result, whose height and width is variable, depending on the occupancy of surface states related to adsorbed species (Capone *et al.* 2003).

There are many wide band gap semiconductors available now a days for different purposes i.e. SiC high temperature applications such as automotive, chemical and petroleum industries, GaN and ZnO-based solid-state (Horsfall *et al.* 2006) sensors. 4H-SiC provides an advantage of reducing the number of electron-hole pairs formed from thermal activation across the band gap, which allows the high-temperature operation of electronic devices, including sensors (Kim *et al.* 2013). Metal-oxide semiconductors became as typical gas sensing elements because of their good sensitivity and reliability. Most metal-oxide semiconductor gas sensors are based on the principle which the sensor reacts with specific gas molecules; the surface of the sensor undergoes certain changes, which in turn result in some changes in the electrical properties of the sensor, such as its resistance or capacitance. Such sensors generally operate at an elevated temperature for maximum performance (Kim *et al.* 2013). Conductometric obviously related to surface reaction. Important parameters for these type gas sensors will change

with the factors influencing the surface reactions, such as chemical components, surface-modification and microstructures of sensing layers, temperature and humidity. Some of the oxides shows a gas response in their conductivity are In_2O_3 , WO_3 , TiO_2 , ZnO (Wang *et al.* 2010). They are also readily integrated with wireless communication circuitry for data transmission. There have seen the greatest interest for chemical gas sensing applications, chiefly for the detection of H_2 , O_2 , NH_3 and ethanol (Pearton *et al.* 2013).

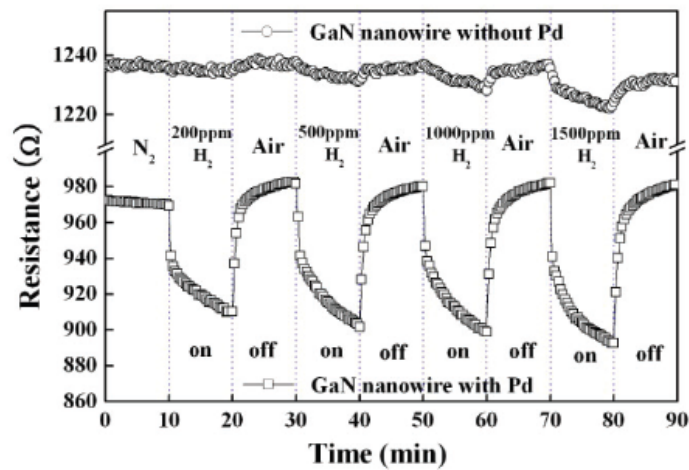


Figure 1.3. Change in resistance of GaN nanowires, either with or without Pd coatings, as a function of gas ambient switched in and out of the test chamber (Pearton *et al.* 2013)

The increase oxidizing reducing gas action makes the resistance of the device, measured in parallel to the surface between ohmic contacts. It is explained that the methodology of fabrication modifies the geometrical and physical parameters of ohmic contacts and the reproducibility of the devices. Influence in ohmic contact resistance for device structures, literature present measurements on contact resistances of ohmic contacts (Al) to n-type MO. The results evaluate the dependence of contact resistances on: the surface and the geometry of the sensitive layer, the process used to attach ohmic contacts (Al) (Berry *et al.* 2007).

Hydrogen becomes important in many fields such as chemicals, petroleum, food and semiconductors industries as we explained before. Because of negative impact in

burning fossils, rising oil price migrated to use of clean energy. Since Hydrogen is an explosive gas Therefore, it is of great importance to detect hydrogen leakages at levels below the lower explosive limit of a 4% volume ratio of hydrogen to air (Kim *et al.* 2013).

As a hydrogen detecting device, the hydrogen sensor is essentially a transducer that transforms the variation of physical or chemical properties into an electrical signal for practical applications. According to the variation of electrical and optical properties of SMOs under a hydrogen-containing atmosphere, the SMO hydrogen sensors can be divided into four types: resistance based, work function based, optical and acoustic sensors (Gu *et al.* 2006). Hydrogen (H_2) is expected to supplant hydrocarbons and becomes “the common fuel of the future”. As it is an invisible, odorless, and flammable gas, it is necessary to detect hydrogen leakage in the environment. There is a strong need to develop novel hydrogen sensors for: solid oxide fuel cells, hydrogen engine cars, transportation and storage of H_2 or other applications. Nowadays, H_2 is used as the fuel for the internal combustion engines and fuel cells that may soon flood into the automotive industry and customers houses due to the potential for substantially cleaner emissions than internal combustion engines. Thus, to control the energy conversion processes in such engines and fuel cells it will require numerous hydrogen sensors for each unit. It is evident that the cost, compactness, reliability and selectivity along with technical requirements on such devices are major specifications which have to be considered when sensors were developed. Also, the importance of development of a nanosensor with ability to selectively detect hydrogen at room temperature is driven by the fact that, in most of the field applications, hydrogen is to be detected at the presence of other combustible gases, such as hydrocarbons and volatile organic compounds, with presence of air in the ambient. Recently the main effort of H_2 sensor development has been the improvement of H_2 gas sensitivity as well as selectivity and to decrease the operating temperature. Compact, reliable, inexpensive, and low power consumption sensor device that can detect hydrogen have been subject of many research groups (Lupan *et al.* 2008).

CO₂ sensing and detection of carbon dioxide (CO₂) gas has attracted attention in the context of global warming, biological and health-related applications such as indoor air quality control, process control in fermentation, and in the measurement of CO₂ concentrations in patients' exhaled breath with lung and stomach diseases. In medical applications, it can be critical to monitor the CO₂ and O₂ concentrations in the circulatory systems for patients with lung diseases in the hospital. The current technology for CO₂ measurement typically uses IR instruments, which can be very expensive and bulky. The most common approach for CO₂ detection is based on non-dispersive infrared (NDIR) sensors, which are the simplest of the spectroscopic sensors (Pearton *et al.* 2006).

Thin film ITO in In₂O₃:Sn (also called indium tin oxide or ITO) highly degenerate heavily doped (Qiao 2003) n-type wide gap semi-conductor (band gap~3.7eV) is a low electrical resistivity (Kerkache *et al.* 2010) well-known transparent conducting oxide (Terzini *et al.* 2013). ITO is transparent but bulk form can change color. ITO, exhibit metal like behavior due to their high conductivities, the films also show high reflectivity in the near infrared region (Qiao 2003).

The current application of ITO films emphasizes the requirement of achieving the lowest possible electrical resistivity with the optimized highest transparency in the visible range. The electrical and optical properties of ITO thin films are critically process dependent. The transparency and conductivity of highly degenerate and wide band gap oxide semiconductor films can be varied by adjusting the deposition conditions. The ability of depositing highly conductive and transparent ITO films is a key issue to obtain the best performance of gas sensor. A large conductivity in an ITO film is accompanied by larger light absorption and opacity. Therefore, an optimized performance is sought for an effective application to gas sensor fabrication.

ITO sensor for H₂ detection based on resistance change mechanism require higher operating temperature that can lead serious safety concerns as H₂ may catch fire in the presence of oxygen. On the other hand, to improve the sensitivity, efforts have been

made to develop nanomaterial for H₂ sensors. Nevertheless, the issues of room temperature sensing with high sensitivity, fast response and recovery times, and high selectivity have not been satisfactorily addressed. Based on the previous literature reports related to the development of integrating indium oxide (In₂O₃) doped tin oxide (SnO₂) nanoparticles for hydrogen sensors to realize a novel material based micro sensor with enhanced sensitivity at room temperature (22°C). Advantages of scaling-down from bulk sensors to micro-machined sensors include increased mass transport rate of the analytes, small sample volume requirement, precise control over the geometry and dimension, which lead to high sensitivity and good repeatability at lower cost. The nanomaterial/micro device integration for a highly efficient sensor device with unprecedented functions has been explored and investigated systematically (Rajnikant *et al.* 2004). The ITO (In₂O₃:SnO₂=20:80) thin films the highest H₂ sensitivity, fast response time and good selectivity compared to the hydrocarbon gases (Yoo *et al.* 2004).

1.2. Thesis Organization

This study exclusively conducted to fulfill the requirement of master studies in nanomaterials. This thesis is mirror of author's capability of learning, understanding, applying, presenting, knowledge sharing and the knowledge transferring. The topic "Developing ITO based gas sensor" selected to learn and experiment to fabricate novel gas sensor device applying fundamental background knowledge of solid state physics and nano science as an application for real life. In this thesis author attempted to provide complete life cycle of prototype ITO gas sensor device fabrication, characterization and testing. Furthermore this experimental study carried out to find new knowledge and method while comparing the outcome with other literature.

This thesis includes fundamental approach to learn and research a gas sensor as a big picture. Before starting the project author developed few hypothesis related to study. We proposed to develop a resistive gas sensor to find performance towards to H₂ gas. Because of ITO having unique properties we selected ITO as a material to design ITO

based H₂ gas sensor i.e. ITO is wide bandgap semiconductor and much more stable than nitride group. We shall explain background theories and practical methods related to developing ITO gas sensor i.e. properties of ITO as gas sensing material, thin film deposition, lithography process, characterization, and testing performance of the ITO sensor towards to H₂ and CO₂.

The aim of this research study is to develop novel metal oxide thin films (ITO) based resistive gas sensors for H₂ sensing applications. This includes investigation of the semiconducting metal oxides with gas chromic properties, deposition or synthesis of the metal oxide thin films onto glass substrate and comprehensive study of the micro-nano characteristics of the metal oxides to understand their influence on the gas sensor's performance. Furthermore investigation of the gas sensing performances developed sensors towards to reducing (H₂) and oxidizing (CO₂) gases.

The study completely based on three hypotheses.

1. Research how the characteristics of the ITO films change when O₂ increase / decrease during the growth?
2. Researches how influence Oxygen partial pressure to improve the sensitivity for different gas specious?
3. Research how geometry and surface volume ratio impact on sensitivity of ITO based gas sensors?

Outcomes and Author's Achievements

This Master Studies research has led to several novel and significant findings contributed to the body of knowledge in the field of gas sensors based on metal oxide thin films. In this thesis, the author presents a comprehensive report on the experiments and the theoretical analysis of the developed gas sensors exposed to H₂ and CO₂ with concentrations at room as well as elevated temperatures. The findings of this research study are several ITO metal oxide based gas sensors that were successfully developed

with excellent sensing performance towards to H₂ gas. Further investigation need to be carried out to testing and improve the device sensing performance. In summary, this Master Studies research program successfully fulfilled its objectives to investigate and develop novel H₂ gas sensors based on ITO thin films.

This thesis consists of 5 chapters. The thesis presentation is outlined as follows:

- Chapter 1 is the introduction and overview of the author's motivation in taking the research in the chemo resistive sensors for gas sensing applications. This includes the background information gas sensor, resistive gas sensor and specialized ITO based H₂ sensor and short information about all the relevant subjects.
- Chapter 2 presents the fundamental theories of research rationales and literature review of the gas sensor for H₂ employing ITO metal oxide gas sensor. Those will be included such as physics of semiconductor based gas sensors, technique/methods, characterization methods etc. The gas sensing properties, mechanism of H₂ and the use ITO as a wide band gap semiconductor for gas sensing applications are also reviewed.
- Chapter 3 outlines all the experimental procedures carried out to design and fabrication, characterization and testing ITO gas sensor. This includes the preparation of the transparent substrates by sputtering technique by optimizing its qualities.
- Chapter 4 presents the experimental results obtained from the developed ITO gas sensors performance towards H₂. The effect of nanostructured materials' morphology, concentrations on the sensors' performance is discussed in great details.
- Chapter 5 including the conclusion.

2. THEORETICAL FUNDAMENTALS

2.1. Gas Sensor

Gas sensors can be divided into categories with reference to its physical changes. There are passive and active sensors: passive sensors provide their own power, for example through exothermic chemical reaction with an analytic, while active devices need an external power source (McGrath 2013).

The process of gas sensing by a semiconductor device involves two key functions as (i) recognition of a target gas through a gas–solid interaction which induces an electronic change of the oxide surface (receptor function) and (ii) transduction of the surface phenomenon into an electrical resistance change of the sensor (transducer function). However, the understanding of these functions is not straightforward, because of the complex nature of the porous, polycrystalline sensing bodies comprising nano-sized grains of semiconducting oxides (Yamazoe *et al.* 1999).

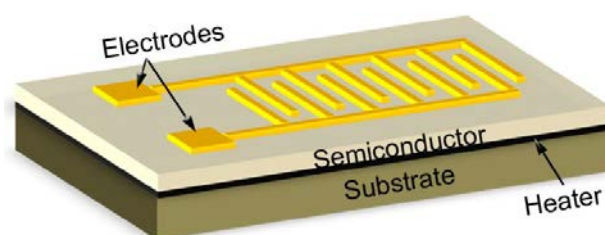


Figure 2.1. Schematic of a resistance based SMO hydrogen sensor (Haoshuang *et al.* 2006)

Chart 2.1. Gas sensors technologies and its measuring parameters

Physical Changes	Type of Device
Electrical Conductivity/Resistivity, $\Delta\sigma/\Delta R$	Conductivity sensors (metal oxide gas sensors, conducting polymers)
Work function, $\Delta\phi$	Field effect gas sensors: diodes, transistors, capacitors
Mass, Δm	Piezoelectric sensors: Quartz crystal microbalances (QMB), surface acoustic wave (SAW), Microcantilevers
Optical Parameters: Reflection, absorption interferometry, fluorescence, refractive index or optical path length.	Optical sensors (fibre optic or thin film)
Heat or temperature, ΔT	Catalytic gas sensors: Seebeck effect, pellistors, semistors
Electromotive force or electrical current in a solid state electrochemical cell	Electrochemical gas sensors (potentiometric or amperometric)

The SMO sensing mechanism for resistance-based is rather complex, and has been investigated by many researchers. The generally accepted mechanism is based on the variation of the surface electron depletion region due to the reaction between hydrogen and the chemisorbed oxygen on the surface. As described in Figure 2.2, under an air atmosphere the oxygen molecules can get adsorbed on the surface of the semiconductor and extracts electrons from the conduction band to form oxygen ions. This process might lead to the formation of an electron depletion region near the surface, which can greatly increase the resistance due to the decrease of net carrier density. When the sensor is exposed to a hydrogen atmosphere, the hydrogen molecules will react with the adsorbed oxygen species. The redox reaction is exothermic and results in the fast desorption of produced H_2O molecules from the surface. The released electrons will reduce the thickness of the depletion region, and decrease the resistance of the semiconductors. When the sensor is exposed to the air ambient again, the depletion region will be rebuilt by adsorbed oxygen species. The resistance will regain the initial level before hydrogen response (Haoshuang *et al.* 2006).

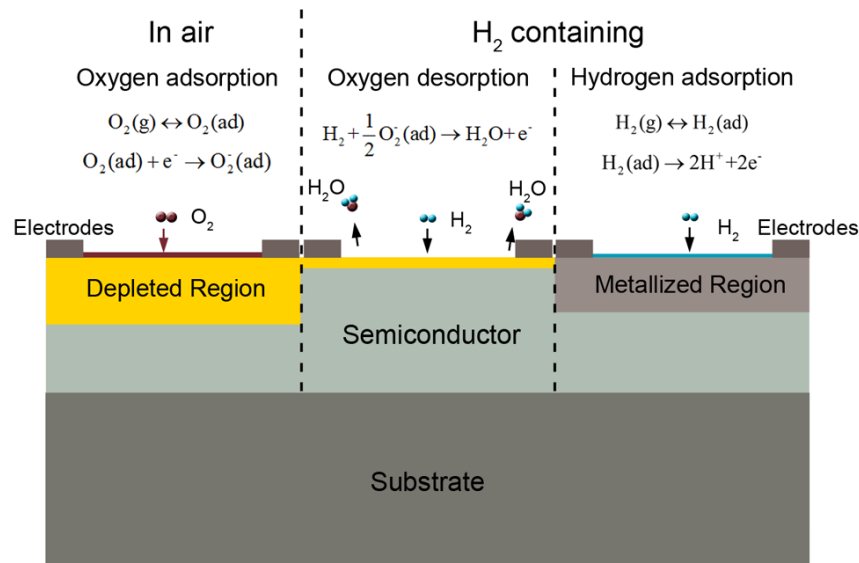


Figure 2.2. Gas sensing mechanism (Haoshuang *et al.* 2006)

Different kind of gas sensors developed with:

- (1) Transition-metal oxides (Fe₂O₃, NiO, Cr₂O₃, etc.)
- (2) Non-transition-metal oxides, which include: (a) pre-transition-metal oxides (Al₂O₃, etc.) and (b) post-transition-metal oxides (ZnO, SnO₂, etc.).

Transition Metal Oxides for Gas Sensors: Many metal oxides are suitable for detecting combustible, reducing, or oxidizing gases by conductive measurements. The following oxides show a gas response in their conductivity: Cr₂O₃, Mn₂O₃, Co₃O₄, NiO, CuO, SrO, In₂O₃, WO₃, TiO₂, V₂O₃, Fe₂O₃, GeO₂, Nb₂O₅, MoO₃, Ta₂O₅, La₂O₃, CeO₂, Nd₂O₃. Metal oxides selected for gas sensors can be determined from their electronic structure.

These type of gas sensors influenced by their properties i.e. solid-state sensors AlGaIn/GaN -high electron mobility transistors, (HEMTs) show a strong dependence of source/drain current on the piezoelectric polarization -induced two dimensional electron gas (2DEG). Furthermore, spontaneous and piezoelectric polarization induced surface and interface charges can be used to develop very sensitive but robust sensors for the

detection of gases, Pt-gated GaN Schottky diodes and $\text{Sc}_2\text{O}_3/\text{AlGaIn}/\text{GaInN}$ metal-oxide semiconductor diodes also show large change in forward currents upon exposure to H_2 containing ambient. AlGaIn/GaN high electron mobility transistors (HEMTs) have demonstrated extremely promising results for use in broad-band power amplifiers in base station applications due to the high sheet carrier concentration, electron mobility in the two dimensional electron gas (2DEG) channel and high saturation velocity. The high electron sheet carrier concentration of nitride HEMTs is induced by piezoelectric polarization of the strained AlGaIn layer and spontaneous polarization is very large in wurtzite III-nitrides. This suggests that nitride HEMTs are excellent candidates for gas sensor applications. However, nitrides are not as thermodynamically stable in oxygen ambient as the oxide semiconductor but oxide doped with aluminum oxide indium-tin-oxide (90% In_2O_3 and 10% SnO_2) are thermodynamically stable (Otto *et al.* 2008).

2.2. Sputtering Technique

If ions or atoms with energy of several kilo-electron volts bombard a solid surface, atoms, molecules or clusters will be produced. Then they can be deposited on the surrounding wall of a vacuum chamber. This process, which is called sputtering, can be used to prepare thin films. Sputtering has many advantages in film deposition. (i) Excellent film uniformity, particularly over large area; (ii) Surface smoothness and thickness control; (iii) The films have strong adhesion and are stable; (iv) Versatility: the sputter process is essentially a kinetic process involving momentum exchange rather than a chemical and thermal process and, therefore, virtually any material can be introduced into a gas discharge or sputtered from the solid; (v) High deposition rate, which is comparable to evaporation.

Normally sputtering processes are divided into four main categories: (i) DC (Direct current); (ii) RF (radio frequency); (iii) magnetron; (iv) reactive. We recognize that there are important variants within each sputtering category (e.g., dc bias technique) and even hybrids between sputtering categories (e.g., reactive RF). However the commonly used sputtering techniques are dc magnetron and RF magnetron sputtering. In all cases

the particles are ejected by the same basic mechanism of momentum exchange between energy particles and surface atoms.

DC method cannot be used to sputter non conducting targets because of charge accumulation on the target surface. This difficult can be overcome by using radio frequency (RF) sputtering. A single RF sputtering apparatus can be used to deposit conducting, semiconducting, and insulating coatings. RF reactive sputtering offers a number of advantages compared with other techniques such as CVD and PVD: it is possible to predict the layer structure and thickness; compound materials may be sputtered roughly without losing the target stoichiometry; good adherence and high film density can be achieved because of the high kinetic energy of the incident target atoms; and uniform layer thickness are obtained (Schmitt and Friedrich 1997).

The technique of RF sputtering uses an alternating voltage power supply at RF frequencies (13.56 MHz), so that the sputtering target is alternately bombarded by ions and then electrons so as to avoid charge build-up. Hence, the insulators can be deposited by RFsputtering. In the case of RF sputtering, the plasma is mainly driven by ionization due to electrons which perform an oscillating motion in the plasma body. The electrons are able to follow the RF frequency of 13.56 MHz while the ions are not, due to their large inertia. This kind of excitation is much more effective compared to the ionization by non-oscillating secondary electrons (in the case of dc-sputtering) and leads to lower target voltages in an RF discharge (Ellmer 2000) and the operating pressure could also be practically extended down to 1 mtorr (Schwartz and Srikrishnan 2006).

The magnetron target is based on the work carried out by penning more than 60 years ago. Since then a lot of work had been done to develop this concept. However, the planar magnetron, which is the most widely used target assembly today, was not introduced until the early 1970s by Chapin (Klabunde 1985). Sputter deposition of thin films for optical and electrical applications has increased markedly in the past few years. This has been mainly a result of the development of high-performance magnetron cathodes. In comparison to conventional diode sputtering, the magnetron cathode

provides higher deposition rates at lower operating pressure and the ability to deposit high-quality films, which with greater adherence and greater uniformity over large areas, at low substrate temperature (Klabunde 1985).

The planar target in its simplest form is shown schematically in Figure 2.3 (b). As comparing the dc diode sputtering process is showed in Figure 2.3 (a). It consists of the target material backed by permanent magnets that provide a toroidal confinement field with the field lines forming a closed tunnel on the target surface. The field strength is chosen to provide effective confinement for electrons while allowing heavier ions considerable freedom.

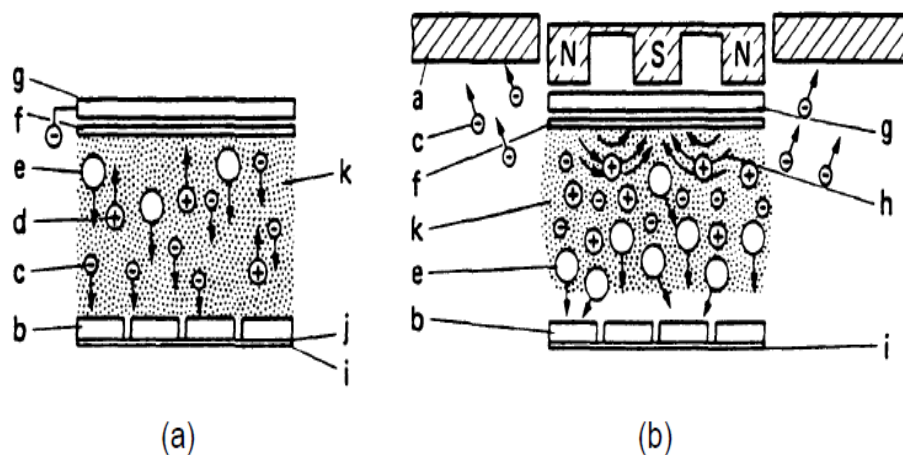


Figure 2.3. Schematic illustrations of the (a) convention dc-diode and (b) planar magnetron cathode sputtering

a. the wall of vacuum chamber, b. substrate, c. secondary electron, d. ion, e. metallic atom, f. target, g. cathode, h. magnet field line, i. substrate holder, j. anode, k. plasma (Qiao aus Hebei 2003)

Secondary electrons emitted from the target during the sputtering process are accelerated across the cathode dark space towards the highly charged plasma sheath. This path is modified by the $E \times B$ Lorentz force. One component of their motion is a helical path about the magnetic field lines. The electrons traveling along these helical lines toward the center of the target are reflected due to the higher density of field lines in this region and the repulsive electric field encountered. After reflection the electrons eventually reach the perimeter of the target where the field lines again intersect the surface. An anode placed in this region effectively collects these electrons and prevents

from reaching the substrate. A second component of their motion is a drift from one field line to another resulting in a race track effect about the toroidal tunnel on the target surface. The combined motion gives an extended path length resulting in a large number of collisions of the electrons with gas atoms. The ions, of course, experience the same Lorentz force as the electrons; however, due to the much higher mass, their motion is not as restricted (Klabunde 1985).

2.3. Indium Tin Oxide

$\text{In}_2\text{O}_3:\text{Sn}$ (also called indium tin oxide or ITO) highly degenerate heavily doped (Zhaohui *et al.* 2003) n-type wide-gap semi-conductor (band gap $\sim 3.7\text{eV}$) is a low electrical resistivity (Kerkache *et al.* 2010) well-known transparent conducting oxide (TCO) (Terzini *et al.* 2000). ITO is transparent but bulk form can change color. ITO, exhibit metal like behavior due to their high conductivities, the films also show high reflectivity in the near infrared region (Zhaohui *et al.* 2003). The current application of ITO films emphasizes the requirement of achieving the lowest possible electrical resistivity with the optimized highest transparency in the visible range. The electrical and optical properties of ITO thin films are critically process dependent. The transparency and conductivity of highly degenerate and wide band gap oxide semiconductor films can be varied by adjusting the deposition conditions. The ability of depositing highly conductive and transparent ITO films is a key issue to obtain the best performance of gas sensor. A large conductivity in an ITO film is accompanied by larger light absorption and opacity. Therefore, an optimized performance is sought for an effective application to gas sensor fabrication.

ITO Crystal Structure: In_2O_3 crystallizes to form the bixbyite structure (also called the C-type rare-earthoxide structure, space group $T_h^7 Ia^3$) (Galasso 1970). The lattice parameter is 1.0117 nm and the density is 7.12 g/cm^3 . Conventional unit cell consists of 16 formula units of In_2O_3 , which shows a fluorite-related superstructure where one fourth of the oxygen anions located along the four $\langle 111 \rangle$ axes are missing. Indium cations are located in two non-equivalent (see Figure 2.4), where 8 In^{3+} ions are located

in the center of trigonal distorted oxygen octahedrons (b site) and the remaining 24 In^{3+} ions are located in the center of the more distorted octahedrons (d site) (Nadaud *et al.* 1998).

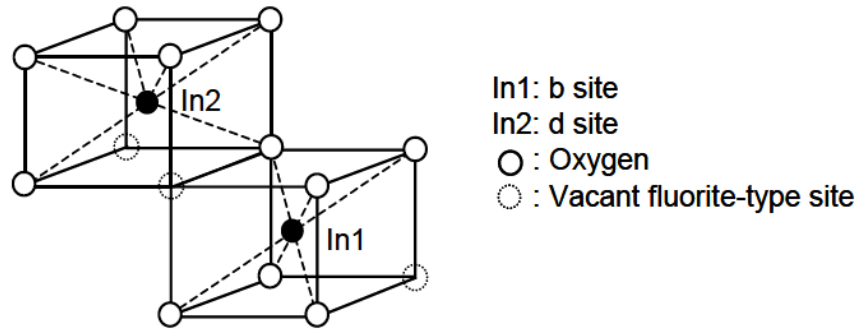


Figure 2.4. Two non-equivalent sites of In atoms in In_2O_3 crystal (Zhaohui 2003)

Indium tin oxide is essentially formed by substitution doping of In_2O_3 with Sn which replaces the In^{3+} atoms from the cubic bixbyite structure of indium oxide. And it was found that tin atoms preferentially occupy the less distorted b lattice sites in the expanded In_2O_3 lattice (Nadaud *et al.* 1998; Yamada *et al.* 1999).

Electrical Properties of ITO Films: Electrical properties of ITO films can be characterized by free carrier density n_e , carrier mobility μ , and electrical conductivity σ or resistivity ρ_e in the films. The relations among these quantities are as follows:

$$\sigma = n_e \mu , \quad (2.1)$$

$$\sigma = 1/ \rho_e, \quad (2.2)$$

Where e is the electron charge. In order to obtain films with high conductivity, high carrier concentration and mobility should be simultaneously realized.

Free Carrier Mobility Scattering mechanisms for ITO films using as transparent electrodes, it is necessary to make a compromise between electrical conductivity and

optical transmittance. Reduction of the resistivity involves either an increase in the carrier concentration or in the mobility. However, increasing the former also leads to an increase in the visible absorption. Hence increasing the mobility is very important for ITO films to achieving high electrical and optical properties. The free carrier mobility μ can be defined as:

$$\mu = e\tau / m_{\text{eff}} , \quad (2.3)$$

Where τ is the average collision time of electrons, m_{eff} is the effective electron mass in conduction band. There are many sources of electron scattering which may influence the mobility, such as ionized impurity scattering, neutral impurity scattering, grain boundary and external surface scattering, acoustical phonon scattering, defect lattice scattering, etc. The scattering mechanisms mentioned above are expected to play different roles in ITO films. For ITO films with good crystallinity, the scattering resulting from the structural disorder can be neglected. Since no remarkable temperature dependence was observed between 100 and 500°C (Bel Hadja Tahar *et al.* 1998), the scattering by acoustical phonons apparently is of a little importance in ITO films.

It is known that grain boundaries act as sites for impurity diffusion and these sites act as scattering centers for carriers. However, for a heavily degenerate semiconductor, the mean free path of electrons is much smaller than the crystallite size (Bel Hadj Tahar *et al.* 1997). Therefore, grain boundary scattering is probably unimportant at high free electron densities. It is reported (Weijtes 1990) that the mobility is determined by grain boundary scattering when carrier density is below $7 \times 10^{20} \text{ cm}^{-3}$. Moreover, the mobility of the free carrier is not affected by surface scattering unless the mean free path is comparable to the film thickness. However, for polycrystalline material, the grain boundary scattering may predominate at very high carrier concentration ($> 1 \times 10^{20} \text{ cm}^{-3}$) due to significant enhancement of the grain boundary potential (Kulkarni and Knickerbocker 1996). It is well-known that the neutral scatter center density increases with increasing Sn concentration (Frank and Köstlin 1982; Bel Hadj Tahar *et al.* 1998).

Band Structure of In_2O_3 is a semiconducting material with a direct band gap of about 3.75 eV and an indirect band gap of about 2.6 eV (Weiher and Ley 1966). The optoelectronic properties of materials are dominated by the electric structure near the band gap. The understanding of the band structure of ITO is based on the theory of In_2O_3 . Some researchers have worked on the electric structure of In_2O_3 and ITO films (Fan and Goodenough 1977; Odaka *et al.* 1997; Odaka *et al.* 2001). But due to its complicated crystal structure, it has not been discovered very clearly so far. According to the theoretical calculation on electronic structure of ITO by Odaka *et al.* (2001), the substitution of Sn atom did not significantly destroy the shape of the density of states around the bottom of the conduction band. The only impurity band locates in the conduction band has the same s-like symmetry as that of conduction band. So the assumed parabolic shape for both valence band and conduction band around the band gap is almost retained independent of the concentration of substitution Sn.

In literatures, several models were used to model the band gap transitions in In_2O_3 or in ITO. All of them incorporated direct allowed transitions. The minimum of the conduction band was assumed to be at $k=0$ (Hamberg and Granqvist 1986) or $k>0$ (Dietrich *et al.* 1984). In order to account for the gradual onset of absorption, an Urbach tail (Hamberg and Granqvist 1986) or indirect forbidden transitions (Sczyrbowski, Dietrich and Hoffmann 1983) were assumed. In the Ref. (Weijtens and van Loon 1991), indirect transition gave a better fit to ellipsometry and reflectance data than an Urbach tail. In direct transition model, the assumed parabolic band structure of undoped In_2O_3 . For undoped In_2O_3 , the Fermi energy E_F is located in the middle of the band gap. The conduction band is empty. With the introduction of a low density of donor atoms, donor states formed just below the conduction band. And the E_F lies between the donor level and the conduction-band minimum. For increased donor density, the donor states merge with the conduction band at a certain critical density n_c , which was calculated to be $2.3 \times 10^{19} \text{ cm}^{-3}$ by Gupta, Mansingh and Srivastava (1989). When $n_e > n_c$ the material expected to exhibit free-electron properties. The intrinsic direct semiconductor band gap is 3.75 eV (Hamberg and Granqvist 1986).

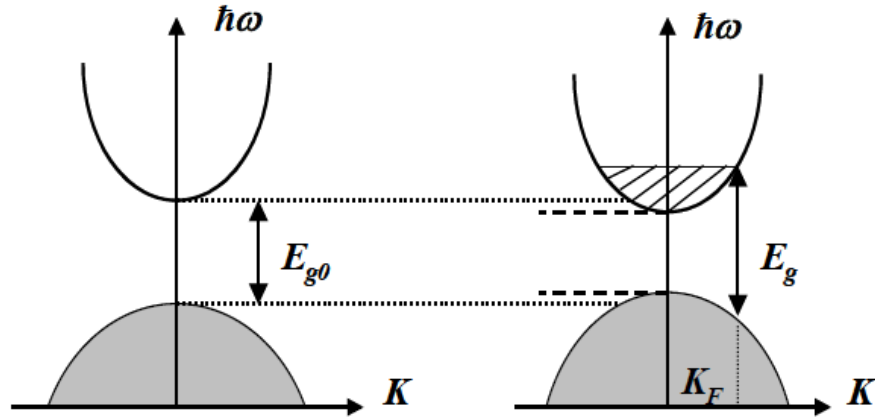


Figure 2.5. Assumed parabolic band structure of undoped In_2O_3 and the effect of Sn doping In ITO films, the fundamental absorption edge shifts towards high energy as the free carrier density increases. The widening of the band gap is known as Burstein- Moss shift (BM) (Burstein 1954; Moss 1954).

2.4. Resistivity and Sheet Resistant

The resistivity ρ of a semiconductor is important for starting material as well as for semiconductor devices. Although carefully controlled during crystal growth, it is not truly uniform in the grown ingot due to variability during growth and segregation coefficients less than unity for the common dopant atoms. The resistivity of epitaxially grown layers is generally very uniform. Resistivity is important for devices because it contributes to the device series resistance, capacitance, threshold voltage, hot carrier degradation of MOS devices, latch up of CMOS circuits, and other parameters. The wafers resistivity is usually modified locally during device processing by diffusion and ion implantation, for example. The resistivity depends on the free electron and hole densities n and p , and the electron and hole mobilities μ_n and μ_p according to the relationship

$$\rho = 1/q(n\mu_n + p\mu_p) \quad (2.4)$$

$$\rho = \frac{\pi}{\ln(2)} t \frac{V}{I} = 4.532t \frac{V}{I} \quad (2.5)$$

ρ can be calculated from the measured carrier densities and mobilities. For extrinsic materials in which the majority carrier density is much higher than the minority carrier density, it is generally sufficient to know the majority carrier density and the majority carrier mobility. The carrier densities and mobilities are generally not known, however. Hence we must look for alternative measurement techniques, ranging from contactless, through temporary contact to permanent contact techniques.

2.5. Two-Point vs Four-Point Probe

The four-point probe is commonly used to measure the semiconductor resistivity. It is an absolute measurement without recourse to calibrate standards and is sometimes used to provide standards for other resistivity measurements. Two-point probe methods would appear to be easier to implement, because only two probes need to be manipulated. But the interpretation of the measured data is more difficult. Consider the two-point probe or two-contact arrangement of Figure 2.6 (a). Each contact serves as a current and as a voltage probe. We wish to determine the resistance of the device under test (DUT). The total resistance R_T is given by

$$R_T = V/I = 2R_W + 2R_C + R_{DUT} \quad (2.6)$$

where R_W is the wire or probe resistance, R_C the contact resistance, and R_{DUT} the resistance of the device under test. Clearly it is impossible to determine R_{DUT} with this measurement arrangement. The remedy is the four-point probe or four-contact arrangement in Figure 2.6 (b). The current path is identical to that in Fig. 2.6(a). However, the voltage is now measured with two additional contacts. Although the voltage path contains R_W and R_C as well, the current flowing through the voltage path is very low due to the high input impedance of the voltmeter (around 10^{12} ohms or higher). Hence, the voltage drops across R_W and R_C are negligibly small and can be neglected and the measured voltage is essentially the voltage drop across the DUT. By using four rather than two probes, we have eliminated parasitic voltage drops, even though the voltage probes contact the device on the same contact pads as the current

probes. Such four contact measurements are frequently referred to as Kelvin measurements, after Lord Kelvin.

An example of the effect of two versus four contacts is shown in Figure 2.6. The drain current–gate voltage characteristics of a metal-oxide-semiconductor field-effect transistor were measured with one contact on source and drain (no Kelvin), one contact on source and two contacts on drain (Kelvin-Drain), two contacts on source and one on drain (Kelvin-Source), and two contacts on source and drain (Full Kelvin). It is quite obvious that eliminating contact and probe resistances in the “Full Kelvin” has a significant effect on the measured current. The probe, contact, and spreading resistances of a two-point probe arrangement on a semiconductor are illustrated in Figure 2.6.

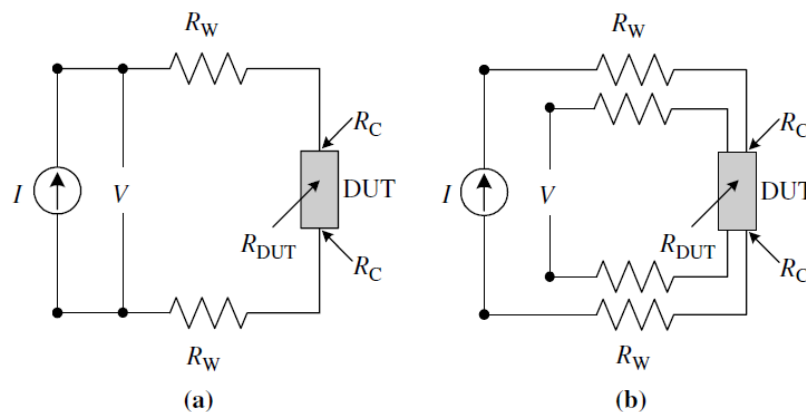


Figure 2.6. Two-terminal and four-terminal resistance measurement arrangements (Schroder 2006)

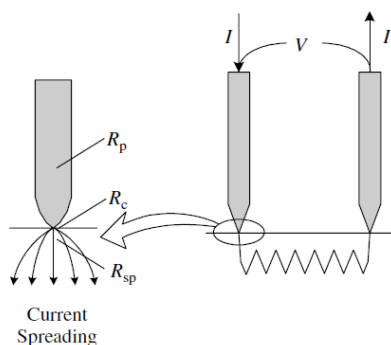


Figure 2.7. Two-point probe arrangement showing the probe resistance R_p , the contact resistance R_c , and the spreading resistance R_{sp} .

The four-point probe was originally proposed by Wenner in 1916 to measure the earth's resistivity. The four-point probe measurement technique is referred to in Geophysics as Wenner's method. Valdes adopted it for semiconductor wafer resistivity measurements in 1954. The probes are generally collinear, i.e., arranged in-line with equal probe spacing, but other probe configurations are possible.

Strengths and Weaknesses of Four-Point Probe: The weakness of the four-point probe technique is the surface damage it produces and the metal it deposits on the sample. The damage is not very severe but sufficient not to make measurements on wafers to be used for device fabrication. The probe also samples a relatively large volume of the wafer, preventing high-resolution measurements. The method's strength lies in its established use and the fact that it is an absolute measurement without recourse to calibrated standards. It has been used for many years in the semiconductor industry and is well understood. With the advent of wafer mapping, the four-point probe has become a very powerful process-monitoring tool. This is where its major strength lies today.

2.6. Metal - Semiconductor Ohmic Contacts

Contact must be made between any semiconductor device or integrated circuit and the outside the world. These contacts made via ohmic contacts. Ohmic contact are metal-to-semiconductor contacts. But in this case they are not rectifying contact. And ohmic contact is a low resistance junction providing conduction in both direction between the metal and the semiconductor. Ideally the current through the ohmic contact is a linear function of applied voltage, and the applied voltage should be very small. Two general types of ohmic contacts are possible: the first type is the ideal non rectifying barrier and the second is the tunneling barrier. We will define a specific contact resistance that is used to characterize ohmic contacts (Neamen 2003).

Some time ago, suggested that the linear current-voltage relationship, e.g. obtained by applying In-electrodes to an n-type CdS-crystal, is due to the easy tunneling of electrons

through a very thin exhaustion barrier between the metal electrode and a thin strongly n-type layer of the crystal underneath the electrode. In spite of the “ohmic” behavior of such contact it is, however, nearly always found that there exists a considerable (“ohmic”) voltage drop near the electrodes, which can be described as being due to an apparent higher specific resistance of the semiconductor material underneath the electrodes. The total resistance of the crystal, when measured directly between the electrodes, is often one or two orders of magnitude higher than when it is measured by means of probes that do not carry an electric current. This apparent contradiction with the model mentioned above, where it was supposed that the region underneath the electrode has a higher specific conductivity than has the bulk of the crystal, can be solved by realizing that most probably the formation of the highly conducting n-type region (e.g. by diffusion of In-metal from the electrode into the CdS at moderate temperatures) will, in general, mainly proceed along narrow paths (dislocations or other crystal faults), in a similar way as has been found with the diffusion of Cu in ZnS crystals at a moderate temperature. The electric current would then follow these spikes, giving rise to an (ohmic) spread resistance in the bulk regions near the spike ends, which could account for the voltage drop near the electrodes. At the same time the field enhancement near these spike-regions would facilitate the tunneling process (Diemer 1960). Ohmic contacts have linear or quasi-linear current-voltage characteristics. It is not necessary, however, that ohmic contacts have linear I–V characteristics. The contacts must be able to supply the necessary device current, and the voltage drop across the contact should be small compared to the voltage drops across the active device regions. An ohmic contact should not degrade the device to any significant extent, and it should not inject minority carriers. The first comprehensive publication on ohmic contacts was the result of a conference devoted to this topic. The theory of metal-semiconductor contacts with emphasis on ohmic contacts was presented by Rideout. Ohmic contacts to III–V devices were reviewed by Braslau and Piotrowska *et al.* 8 and ohmic contacts to solar cells were discussed by Schroder and Meier. Yu and Cohen have presented discussions of contact resistance (Schroder 2006).

2.7. Absorption

Nonmetallic materials may be opaque or transparent to visible light; and, if transparent, they often appear colored. In principle, light radiation is absorbed in this group of materials by two basic mechanisms, which also influence the transmission characteristics of these nonmetals. One of these is electronic polarization. Absorption by electronic polarization is important only at light frequencies in the vicinity of the relaxation frequency of the constituent atoms. The other mechanism involves valence band-conduction band electron transitions, which depend on the electron energy band structure of the material; band structures for semiconductors and insulators. Absorption of a photon of light may occur by the promotion or excitation of an electron from the nearly filled valence band, across the band gap, and into an empty state within the conduction band.

By “optical property” is meant a material’s response to exposure to electromagnetic radiation and, in particular, to visible light. This chapter first discusses some of the basic principles and concepts relating to the nature of electromagnetic radiation and its possible interactions with solid materials. Next to be explored are the optical behaviors of metallic and nonmetallic materials in terms of their absorption, reflection, and transmission characteristics.

Nonmetallic materials may be opaque or transparent to visible light; and, if transparent, they often appear colored. In principle, light radiation is absorbed in this group of materials by two basic mechanisms, which also influence the transmission characteristics of these nonmetals. One of these is electronic polarization. Absorption by electronic polarization is important only at light frequencies in the vicinity of the relaxation frequency of the constituent atoms. The other mechanism involves valence band-conduction band electron transitions, which depend on the electron energy band structure of the material; band structures for semiconductors and insulators. Absorption of a photon of light may occur by the promotion or excitation of an electron from the

nearly filled valence band, across the band gap, and into an empty state within the conduction band.

2.7.1. Quantities for semiconductor spectroscopy (Reflectance, Transmittance and absorbance)

Know about frequency-dependent dielectric function of a solid means knowing microscopic optical response. Light shines on the surface of a sample usually a slab with a flat faces. Standard spectroscopy empowers for infrared, measures the amount of light reflected at the front surface, or transmitted through the back side of surface. That depends on the geometry of the sample. In photoluminescence and Raman Spectroscopy are not measured reflectance and transmittance. It is important to determine the condition and meaning of the measurement of behaviors of the light at the air semiconductor interfaces. In a spectroscopy imaging electromagnetic waves effected from each interface between different materials if a semiconductor having many layers.

Always boundary conditions determine behavior of electromagnetic waves of an interface. This can explain by Maxwell's partial diffraction equation. Slab incident light reflected at an interface between two materials of single type semiconductor. Angle of incident is depend in reflects and transmittance at any angle other than normal incidence, the behavior of the interface also depends on the polarization light.

$$\alpha = \frac{2\omega k}{c} = 4\pi f k \quad (2.7)$$

$$\frac{(1-R)^2 e^{-\alpha d}}{1-R^2 e^{-2\alpha d}} = e^{-A} \quad (2.8)$$

Absorption coefficient α is the fractional change in intensity per unit length of penetration due solely to absorption in the semiconductor. α Can be found from equation 2.8 when absorption R and d thickness known (Perkowiitz 1993)

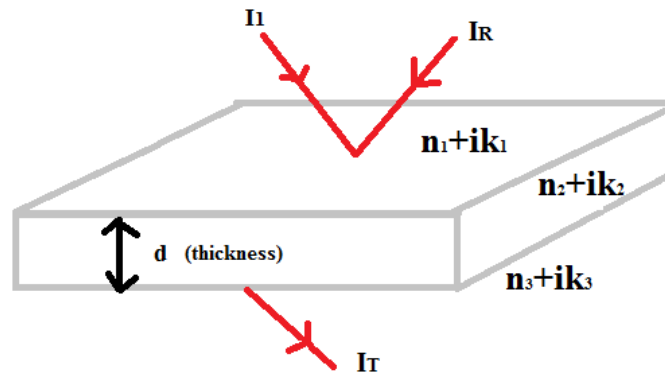


Figure 2.8. Showing incident, reflected and transmitted intensities

2.7.2. UV-Vis-NIR Spectrophotometry and band gap analysis

Ultraviolet-visible-near infrared (UV-Vis-NIR) spectrophotometry is a characterization technique based on the interaction of electromagnetic waves in the UV-Vis-NIR wavelength ranges and the material the magnitude of the absorbed or emitted electromagnetic waves by the materials is analyzed against the wavelengths. Information on the material's optical properties such as transparency and optical band gap can be extracted from this spectrum. The UV-Vis-NIR spectrophotometry system consists of light sources to produce light of a known intensity and wavelength ranges onto material and a spectrophotometer to measure the spectrum and intensity of the light exiting the material. According to Tauc equation, the band gap can be estimated from the following expression:

$$\alpha h\nu = A(h\nu - E_g)^n \quad (2.9)$$

where α is the absorption coefficient, h is Planck's constant (1.69×10^{-19}), ν is the photon frequency ($3 \times 10^8 \text{ ms}^{-1}$), A is the dimensional constant, E_g is the energy band gap and n is 2 for indirect semiconductor such as WO_3 . Based on this equation, the estimation of the energy band gap was obtained by plotting $(\alpha h\nu)^2$ versus photon energy ($h\nu$). The estimated optical band gap is the value of the linear extrapolation of the plotted curve (Mohd 2012).

2.7.3. Energy band gap (E_g)

In the strong and medium absorption region, the optical behavior of the films is dominated by the absorption from the valence electrons. The absorption coefficient α can be determined by: $\alpha^N = C (h\nu - E_g)$, where N is dependent on the type of electron transitions, and E_g is the band gap. In case of direct and indirect transition semiconductor, N is 2 and 1/3 respectively. From the absorption data, it is then possible to obtain E_g for each film. There are different models and many reports about the absorption coefficient. α is obtained from measurements of the absorption spectrum. If α^2 is plotted vs. the photon energy ($h\nu$), extrapolating the linear region towards the $h\nu$ axis gives the effective direct transition energy E.

For probing the band structure in semiconductors, one of the most direct methods is the optical absorption studies. We can determine the optical band gap of a material as well as determine whether the valence band and conduction band extrema occur at the same or different points in the k-space, knowing the frequency dependence of the absorption processes such as fundamental absorption, free carrier absorption, excitonic absorption and impurity absorption. Electrons can be excited from the valence band to the conduction band with the absorption of a photon of energy equal to the band gap of the material. Rapid drop in the absorption coefficient on the higher energy side of the absorption band leads to the band edge in semiconductors which can be analyzed to get the optical band gap energy of the material. The metal phthalocyanines belong to the point group D_{4h}, and the electronic structure of metal phthalocyanines was described by Gouteman and coworkers. Charge transfer and electron absorption studies of metal phthalocyanine by YOS hida' *et al.* suggests the effect of hybridisation between intermolecular excitations. Fundamental information on the molecular structure of solid films can be obtained by analysis of their molecular spectra. Molecular solid films are assemblies of organic molecules loosely bound together by Van der Waals type of interaction.

2.8. Determining the Structure of ITO Films by X-ray Diffraction

X-ray diffraction (XRD) is a very important experimental technique in revealing the crystal structure of bulk solid microstructure of thin films. The XRD methods are generally applied to films thicker than several angstroms on account of the strong penetrating power of the x-ray. Many information related to the crystal structure of the films, including lattice constants, grain size, preferred orientation of poly crystals, defects, stress, etc. can be determined from the x-ray diffraction measurement. X-rays are electromagnetic waves. The phenomenon of the x-ray diffraction by crystals results from a scattering process in which x-rays are scattered by the electrons of the atoms without change in wavelength. A diffracted beam is produced by such scattering only when certain geometrical conditions are satisfied, which may be expressed in either of two forms, the Bragg law or the Laue equations. The resulting diffraction pattern of a crystal, comprising both the positions and intensities of the diffraction effects, is a fundamental physical property of the substance. Analysis of the positions of the diffraction effect leads immediately to a knowledge of the size, shape and orientation of the unit cell.

2.9. Scanning Electron Microscopy (SEM)

SEM is the main technique used in this project to characterize the morphologies of the materials. A scanning electron microscope consists of an electron optical column, a vacuum system and electronics. The column comprises of an electron source to produce electron beam, a set of lenses to focus the electrons into a fine spot onto the samples in the specimen chamber and a secondary electron detector to convert the scanned beam into electrical signal for image processing. These devices are encapsulated in a vacuum system which allows primary electrons movement in straight lines and operates in low or high vacuum modes. The electronic circuitries are mainly employed to control the voltages and currents for the electron source, magnetic lenses and the detector. High resolution images can only be produced by SEM if the samples are conductive. Electric

charging occurs for samples with minimum or no conductivity. This can be prevented by coating the samples with a thin layer of Pt or Au (10-50Å) via DC sputtering.

2.10. Etching

Different etching processes are selected depending upon the particular material to be removed. Wet chemical processes result in isotropic etching where both the vertical and lateral etch rates are comparable, whereas dry etching processes like sputter etching, plasma etching, ion beam etching, and reactive ion etching are anisotropic. Among the dry etching techniques, plasma and reactive ion etching are the most popular in semiconductor processing (Paul 2005). Wet chemical etching is used for lapping and polishing to give an optically flat, damage-free surface. Prior to thermal oxidation or epitaxial growth, wafers are chemically cleaned and scrubbed to remove contamination that results from handling and storing. For many discrete devices and integrated circuits of relatively large dimensions ($>3 \mu$), chemical etching is used to delineate patterns and to open windows in insulating materials. In fabrication processing, most chemical etchings proceed by dissolution of a material in a solvent or by converting the material into a soluble compound that subsequently dissolves in the etching medium. As illustrated in Figure 2.9, wet chemical etching involves three essential steps:

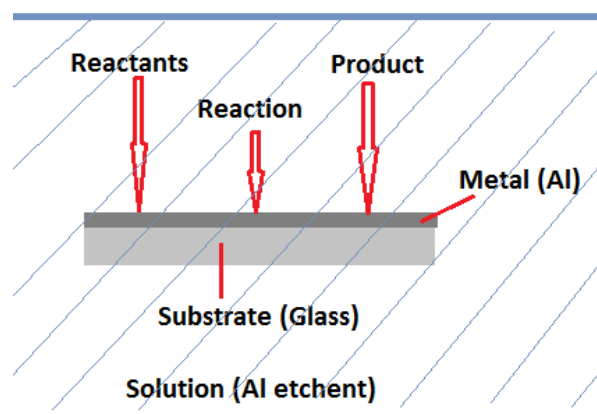
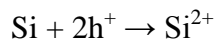


Figure 2.9. Basic mechanisms in wet chemical etching

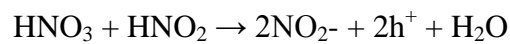
- (1) Transportation of reactants to the reacting surface (e.g. by diffusion)
- (2) Chemical reactions at the surface
- (3) Transportation of the products from the surface (e.g. by diffusion)

For semiconductor materials, wet chemical etching usually proceeds by oxidation, accompanied by dissolution of the oxide. For silicon, the most commonly used etchants are mixtures of nitric acid (HNO₃) and hydrofluoric acid (HF) in water or acetic acid

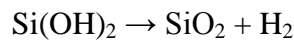
(CH₃COOH). The reaction is initiated by promoting silicon from its initial oxidation state to a higher oxidation state:



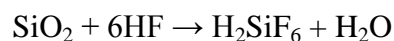
The holes (h⁺) are produced by the following autocatalytic process:



Si²⁺ combines with OH⁻ (formed by the dissociation of H₂O) to form Si(OH)₂ which subsequently liberates H₂ to form SiO₂:



SiO₂ then dissolves in HF:



The overall reaction can be written as:



Although water can be used as a diluent, acetic acid is preferred as the dissociation of nitric acid can be retarded in order to yield a higher concentration of the dissociated species.

At very high HF and low HNO₃ concentrations, the etching rate is controlled by HNO₃, because there is an excess amount of HF to dissolve any SiO₂ formed. At low HF and high HNO₃ concentrations, the etch rate is controlled by the ability of HF to remove SiO₂ as it is being formed. The latter etching mechanism is isotropic, that is, not sensitive to crystallographic orientation. Etching of insulating and metal films is usually performed with the same chemicals that dissolve these materials in bulk form and involves their conversion into soluble salts and complexes. Generally film materials will etch more rapidly than their bulk counterparts. Moreover, the etching rates are higher for films that possess poor microstructures or built-in stress, are non-stoichiometric, or have been irradiated (Chu 2005).

3. MATERIALS and METHODOLOGIES

3.1. Cleanroom

This study conducted in the clean room facilitated by nano fabrication laboratory, University of Manitoba and the Solid state Physics Laboratory Ataturk University after the successful clean room training. In a clean room, the total number of dust particles per unit volume must be strictly controlled along with other parameters such as temperature, humidity, pressure, and so on. A class X clean room is usually defined to be one that has a dust count of X particles (diameters of $0.5\ \mu\text{m}$ or larger) per cubic foot. As shown in Figure 3.1, 3.2, the particle count is higher as the particle size becomes smaller. For modern lithographic processes, a class 10 or better cleanroom is required. All cleanroom users are required to pass cleanroom training.

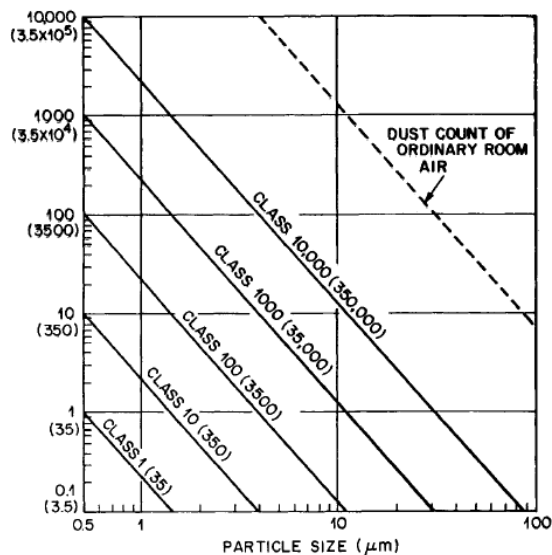


Figure 3.1. Particle-size distribution curve (Chu 2005)

In our study for device fabrication requires a clean room, particularly in lithography areas. Dust particles settling on semiconductor wafers and lithographic masks can cause defects in the devices. As shown in Figure 3.2, airborne particles adhering to the surface of a photo mask behave as opaque patterns that can be subsequently transferred to the

circuit patterns. For example, particle 1 in Figure 3.2 may result in the formation of a pinhole in the underlying layer. Particle 2 may cause a constriction of current flow in the metal runner, whereas particle 3 may lead to a short circuit between the two conducting regions and render the circuit useless (Chu 2005).

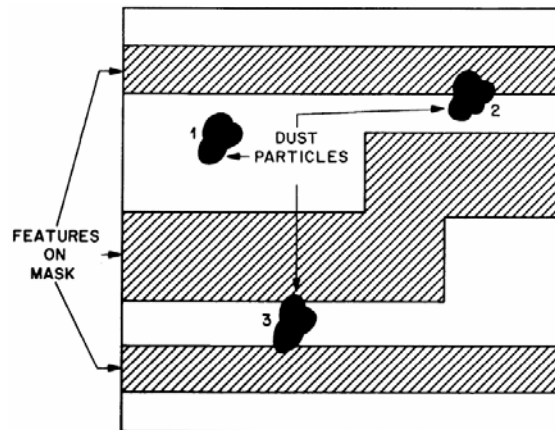


Figure 3.2. How dust particles can interfere with photo mask patterns

3.2. RF/DC Magnetron Sputtering System



Figure 3.3. MRC 8667 RF/DC sputtering system

Sputter deposition is a physical vapor deposition process for depositing thin films, sputtering means ejecting material from a target and depositing it on a substrate such as a silicon wafer. The target is the source material. Substrates are placed in a vacuum chamber and are pumped down to a prescribed process pressure. Sputtering starts when a negative charge is applied to the target material causing a plasma or glow discharge. Positive charged gas ions generated in the plasma region are attracted to the negatively biased target plate at a very high speed. This collision creates a momentum transfer and ejects atomic size particles from the target. These particles are deposited as a thin film into the surface of the substrates.

Sputtering is extensively used in the semiconductor industry to deposit thin films of various materials in integrated circuits processing. Thin anti reflection coatings on glass, which are useful for optical applications are also deposited by sputtering. Because of the low substrate temperatures used, sputtering is an ideal method to deposit contact metals for thin - film transistors. This technique is also used to fabricate thin film sensors photovoltaic thin films solar cells, metal cantilevers and interconnects etc. Magnetron sputtering can be done either in DC or RF modes. DC sputtering is done with conducting materials. If the target is a non-conducting material the positive charge will build up on the material and it will stop sputtering. RF sputtering can be done both conducting and non-conducting materials. Here, magnets are used to increase the percentage of electrons that take part in ionization of events and thereby increase the probability of electrons striking the Argon atoms, increase the length of the electron path, and hence increase the ionization efficiency significantly i.e. max rf power 500W, dc power 200w, Sputtering total pressure 16mT, roughing pump 50 mT.

3.3. Substrate Cleaning

There can be use many kind of substrate for thin film deposition such as Si wafer, Ceramic, Quartz, Soda lime or Sapphire glass. Throughout our study we used 2"x3" glass for thin film deposition and sensor device fabrication. Typical contaminants removed prior to deposition and lithography of the samples used in the device

fabrication. Throughout the study we followed several cleaning procedures to clean substrate and equipment.

The glass substrate cleaned by piranha solution using is 4:1 $\text{H}_2\text{SO}_4:\text{H}_2\text{O}_2$. The cleaning time is 10 minute, but usually 5 minute is sufficient before the process. Sample prepared for the thin film deposition cleaned by degased one minute and 60 minute ultrasonic bath in the DI water then rinsed with acetone, followed by cleaning IPA, DI water and drying with nitrogen gas blow off. After that samples dried on the hot plate at 110°C for the 30 minutes duration. Nitrogen blow off dry and IPA solution used for clean sample holders tools and chucks whenever required.

Prior to the deposition of the thin films, the substrates were cleaned to remove particles and contaminants on the surface. Initially the substrates were washed in acetone for three minutes to remove organic impurities before rinsed in isopropanol (IPA) and methanol. Later, de-ionized (DI) water was used to soak the substrates from the solvents. Finally, the substrates were blown dry in nitrogen (N_2).

3.4. ITO Thin film Deposition

ITO thin films were grown onto the glass substrate by deposition MRC 8667 model four target RF/DC magnetron sputtering system from a ITO (99.99%), 14 cm metal target in O_2 and Argon atmosphere using RF magnetron source in a turbo molecular pumped stainless steel chamber. The substrate was in room temperature during deposition, typically. The films are grown in different O_2 fractions to the total pressures in the growth environment such as pure ITO, ITO rich, ITO moderate, and O-rich. In order to check the reproducibility of the samples, two thin films were grown in each sample at the same growth conditions. Thin films having the same growth conditions showed almost the same optical and structural characteristics and sensitivity. We experimentally found favorable growth conditions for our prototype gas sensors. The all target we used 14 cm diameter. In this system the best suited power for our experiment ITO deposition RF 300 W (to get proper plasma glow) and 15 minutes time duration (obtain required

thickness). After growth the thin film thickness found by Alfa step profilometer and measured sheet resistance and resistivity by four probe resistivity measuring system. Growth parameters are given in Chart 3.1. We adjusted the Argon and O₂ percentage to be form ITO by according to the sputter total pressure as the formulae 3.1.

$$\text{O2 Percentage \%} = \frac{\text{O2(sccm)}}{\text{Ar (sccm)+ O2(sccm)}} \times 100 \quad (3.1)$$

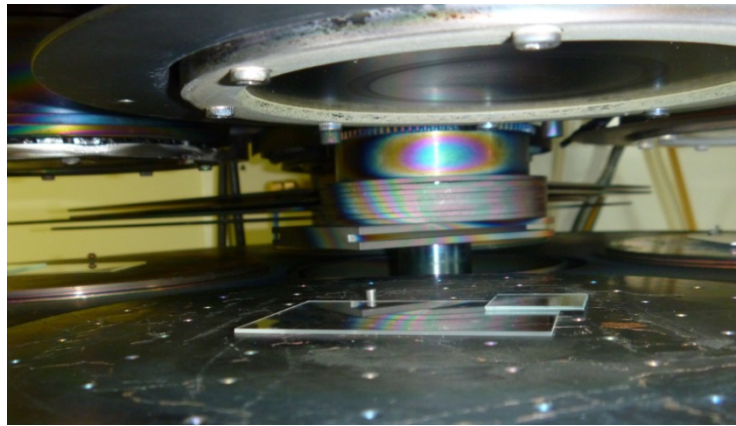


Figure 3.4. ITO loaded and ready for sputtering



Figure 3.5. 14 cm 99.99% purity ITO target

Chart 3.1. Growth conditions for ITO thin film

Chamber 1 Set up Conditions	Chamber 2 Setup Conditions
$P_{\text{Base}} = 2.8 \times 10^{-6} \text{Torr}$	$P_{\text{Base}} = 6.0 \times 10^{-6} \text{Torr}$
$P_{\text{Total}} = 9.7 \times 10^{-3} \text{ to } 9.9 \times 10^{-3} \text{Torr}$	$P_{\text{total}} = 9.7 \times 10^{-3} \text{ to } 1.0 \times 10^{-2} \text{Torr}$
Power= 300W	Power= 300W
Target d= 14 cm	Target d= 14 cm
offset : Ar – 2.1, O ₂ - 1.7	Offset: Ar – 0.2, O ₂ - 1.4
15 minutes for all Samples 1-4	15 minuts for all Samples 5-8

Chart 3.2. Summarized conditions and results of ITO growth

Sample No	Time	Ar sccm	O ₂ sccm	O ₂ %	Sheet Resistance SQ-cm	Thickness nm
1	15	55.7	15.1	21.3	1.925×10^4	885
2	15	66.1	8.8	11.74	1.025×10^5	250
3	15	71.6	2.0	2.7	1.182×10^5	983
4	15	51.0	17.0	25	-	403
5	20	61.4	12.0	16.3	1.543×10^5	900
6	20	63.6	9.9	13.5	2.39×10^5	335
7	15	66.4	7.1	9.6	1.632×10^5	258
8	15	70.2	5.2	6.9	3.18×10^5	543
9	15	66.1	8.8	11.74	2.06×10^5	663
10	15	66.1	8.8	11.74	3.8×10^5	1002
11	15	61.4	12.0	16.3	7.34×10^4	825
Pure	5	74.0	0.0	0.0	-	333

Chart 3.3. Growth conditions for ITO device

Chamber 1 Conditions ITO 1 & 2 Devices	Chamber 2 Conditions ITO 3 & 4 Devices	Chamber 3 Conditions ITO 5 Device
$P_{\text{Base}} = 3.0 \times 10^{-6} \text{ Torr}$	$P_{\text{Base}} = 3.5 \times 10^{-6} \text{ Torr}$	$P_{\text{Base}} = 9.3 \times 10^{-6} \text{ Torr}$
$P_{\text{Sutter}}(\text{total}) = 9.7 \times 10^{-6}$ to $1.0 \times 10^{-2} \text{ Torr}$	$P_{\text{s}}(\text{total}) = 9.7 \times 10^{-3} \text{ Torr}$ to $1.0 \times 10^{-2} \text{ Torr}$	$P_{\text{s}}(\text{total}) = 9.7 \times 10^{-3} \text{ Torr}$ to $1.0 \times 10^{-2} \text{ Torr}$
Power= 300W	Power= 300W	Power= 300W
ITO Target d= 14 cm	ITO Target d= 14 cm	ITO Target d= 14 cm
offset Ar – 1.9, O ₂ - 1.7	offset Ar – 2.0, O ₂ - 1.4	offset Ar – 1.9, O ₂ - 1.6
Time : 15minuts	Time 15 minutes	Time 15 minutes

Chart 3.4. Prescribed Ar and O₂ percentages for ITO device

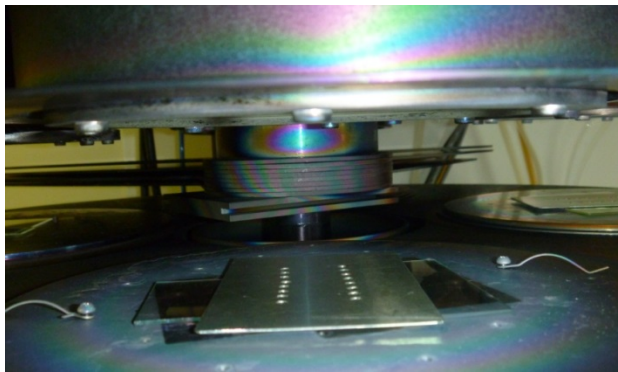
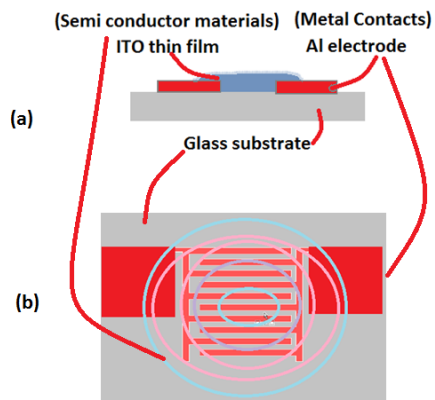
Device	Time	Ar sccm	O ₂ sccm	O ₂ %
ITO 1	15	65.9	8.9	11.9
ITO 2	15	65.9	8.9	11.9
ITO 3	15	61.4	61.4	16.3
ITO 4	15	63.7	9.9	13.5
ITO 5	15	74.4	0.0	0.0

3.4.1. Al Deposition for Metal Electrode of the Gas Sensor

We deposited Al thin film expected 500nm thickness. After removing Al thin film deposited on the glass substrate from the sputter we measured the Al thickness to ensure the thickness 500nm reached by Alfa step 500 profilometer Ver 1.7.91 by giving scan length 500 μm , scan direction \leftarrow and range 13 $\mu\text{m}/1 \text{ \AA}$.

Chart 3.5. Sputter chamber conditions and desired recipe for the Al thin film

P_{Base} (Torr)	P_{Sputter} (Torr)	Argon (sccm)	Power DC Watt	Time	Thickness
3.5×10^{-6}	3.5×10^{-3}	69.1	200 W	8 min.	560nm

**Figure 3.6.** The patterned Al glass substrate mounted in the RF sputtering system to deposit ITO thin film using shadow/tensile mask**Figure 3.7.** ITO deposited thin film device (a) cross sectional (b) schematic view under the optical microscope (c) Physical ITO deposited device under microscope

3.5. Photo Lithography

Photolithography is an optical means for transferring patterns onto a substrate. It is essentially the same process that is used in lithographic printing. Patterns are first transferred to an image capture photoresist layer. Photoresist is a liquid film that can be spread out onto a substrate, exposed with a desired pattern, and developed into a selectively placed layer for subsequent processing. Photolithography is a binary pattern transfer so there is no gray scale, color, nor depth to the image (Paul 2005). The vast majority of lithographic equipment for fabrication is optical equipment using ultraviolet light ($\lambda \cong 0.2 \mu\text{m}$ to $0.4 \mu\text{m}$) or deep ultraviolet light. Shadow printing and projection printing are the basic two optical exposure methods.

A photoresist is a radiation sensitive compound. For positive resists, the exposed region becomes more soluble and thus more readily removed in the developing process. The net result is that the patterns formed in the positive resist are the same as those on the mask. For negative resists, the exposed regions become less soluble, and the patterns engraved are the reverse of the mask patterns.

A positive photoresist consists of three constituents which are a photosensitive compound, a base resin, and an organic solvent. Prior to exposure, the photosensitive compound is insoluble in the developer solution. After irradiation, the photosensitive compound in the exposed pattern areas absorbs energy, changes its chemical structure, and transforms into a more soluble species. Upon developing, the exposed areas are expunged. Negative photoresists are polymers combined with a photosensitive compound. Following exposure, the photosensitive compound absorbs the radiation energy and converts it into chemical energy to initiate a chain reaction, thereby causing crosslinking of the polymer molecules. The cross-linked polymer has a higher molecular weight and becomes insoluble in the developer solution. After development, the unexposed portions are removed. One major drawback of a negative photoresist is that the resist absorbs developer solvent and swells, thus limiting the resolution of a negative photoresist.

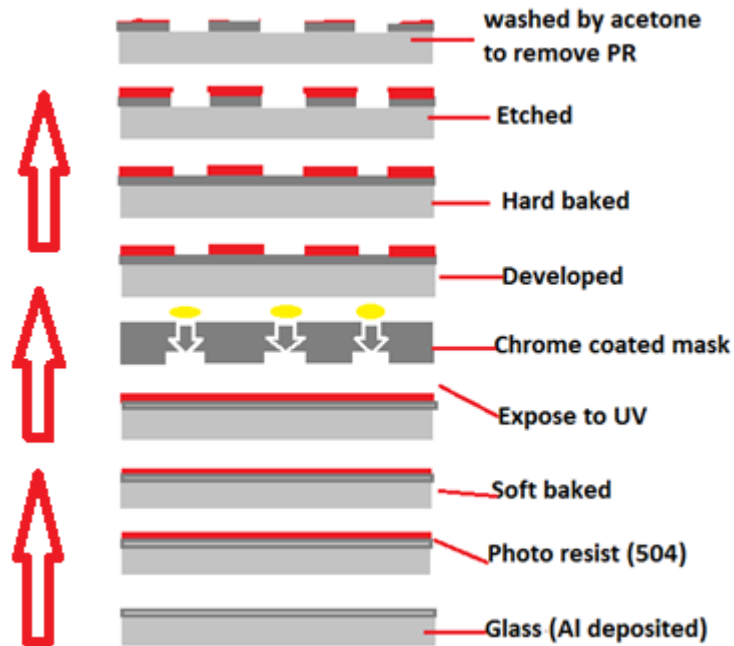


Figure 3.8. Simple lithographic process schematic summary

After examined some scientific literature we selected three type of patterns and three different sizes ($\frac{1}{4}$ mm, $\frac{1}{2}$ mm, 1 mm) to design for image of gas sensor device. Our focus was to give geometrically good surface volume ratio for the sensor device to enhance resistance. We designed the photo mask using computer aid L-edit standard cad tool supported software from Tanner EDA. A photo mask is a piece of glass that you will use to transfer your design to a material layer that you wish to pattern for further processing. The physical properties of each mask fabricated at the NanoFab, University of Alberta 5" x 5" soda lime glass 0.09" thick Chrome coated (approx. 70nm thick). We determined the polarity of mask. Inverted (polygons=chrome) vs. Non-Inverted (polygons=glass) as we used 504 positive PR.

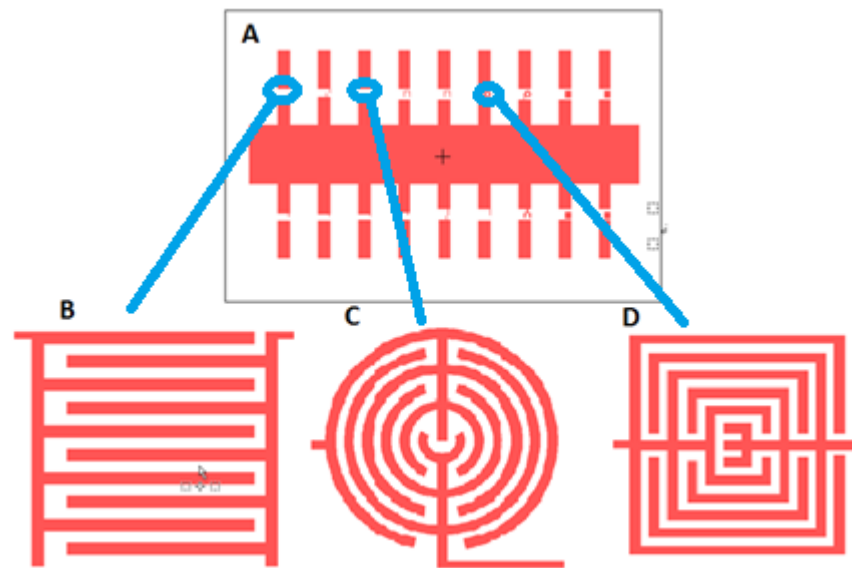


Figure 3.9. Computer aid photo mask image

According to the availability of laboratory resources two different physical masks designed in the University of Alberta and the Bilkent University.

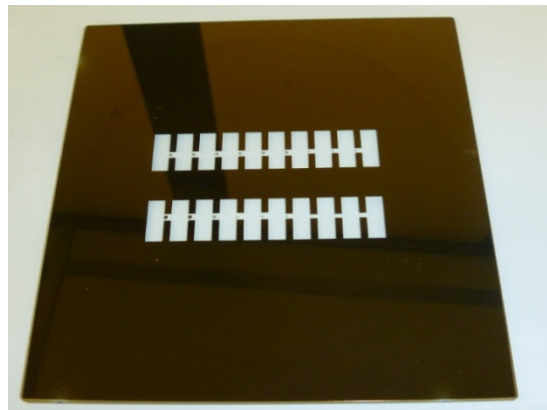


Figure 3.10. Chrome coated glass physical photo mask

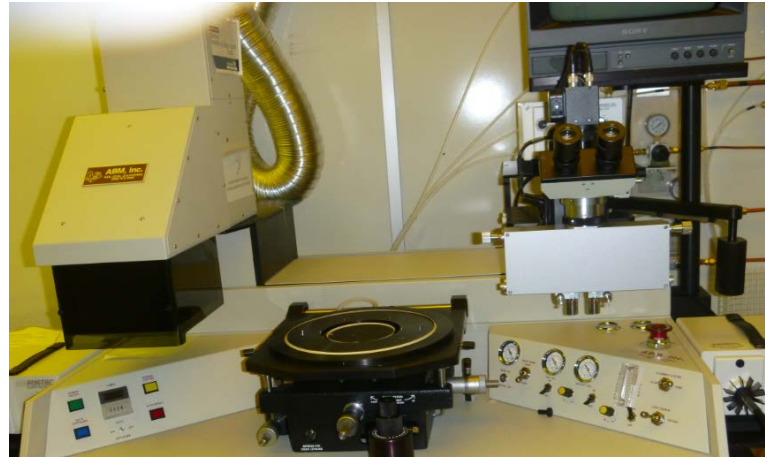


Figure 3.11. Mask Aligner

Al coated glass substrate is held on a spinner chuck by vacuum and resist is coated to uniform thickness by spin coating (3000-6000 rpm for 15-30 seconds).

Resist thickness is set by:

1. Primarily resist viscosity
2. secondarily spinner rotational speed

Resist thickness is given by $t = kp^2/w^{1/2}$, where k = spinner constant, typically 80-100, p =resist solids content in percent w =spinner rotational speed in rpm/1000 Most resist thicknesses are 1-2 μm for commercial Si processes.

500nm Al sputtered thin film 2"x3" glass substrate moisture by DI water. Soft baker tested for glass substrate surface temperature as it designed for Si substrate. Soft baker adjusted temperature 110°C for 2 minutes for the glass substrate and because of Al cooling very fast. Reasonable amount of 504 PR spread over Al deposited glass substrate by the spine coating. Resist 50/50 500 RAMO for 10 seconds, Spread 100 for 10 seconds and spine 300 for 30 seconds. We measured the thickness of Al thin film after deposition it varied from 200nm to 900nm. Photo resist thickness varied from 1.700 μm to 3.1 μm . Prebake (soft bake) used to evaporate the coating solvent and to

densify the resist after spin coating. A narrow time-temperature window is needed to achieve proper line width control. The thickness of the resist is usually decreased by 25% during prebake for both positive and negative resists. We kept 504 PR coated sample glass under 210°C in soft bake hot plate for 2 minutes. The glass moisture by DI water and dried by N₂ gas blow. The 504 PR coated glass kept on mask aligner holder and mounted the photo mask top of the glass holder then exposed 5 seconds for UV light. Developer arranged to the 10 second pre wet, 20 second develop, 10 seconds dwell, 20 second rinse and 20 second spine.

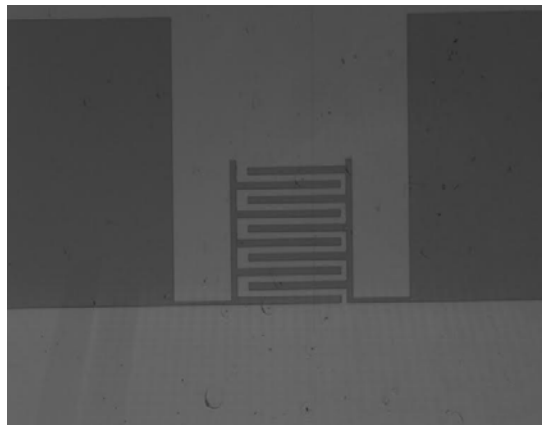


Figure 3.12. Photo resisted, UV exposed, developed glass substrate under optical microscope

Post Bake used to stabilize and harden the developed photoresist prior to processing steps that will resist transferred pattern. Main parameter is the plastic flow or glass transition temperature. Post bake removes any remaining traces of the coating solvent or developer. This eliminates the solvent burst effects in vacuum processing. Post bake introduces some stress into the photoresist so some shrinkage of the photoresist may occur. Longer or hotter post bake makes resist removal much more difficult. Photoresist will undergo plastic flow with sufficient time and/or temperature. We kept the lithographed glass in hard baker (post bake) at least for 30 minutes at 110°C after we confirmed the patterns transfer in to the glass as we expected.

Two primary techniques for patterning additive and subtractive processes are etch-back: photoresist is applied overtop of the layer to be patterned unwanted material is etched away and lift-off: patterned layer is deposited over top of the photoresist unwanted material is lifted off when resist is removed. We followed etch back method to etch unwanted Al film. We cleaned out the Al thin film UV exposed areas of the glass substrate using the Al etch solution (Chart 3.6) which heated 70°C, 138 Rpm rotating and on the 134 heated hot plate for two (2) minutes in the acid wet deck cleansed by DI water immediately and followed drying by N₂ gas. After etching the Al of the well dried glass substrate removed the PR by acetone in lithography wet deck.

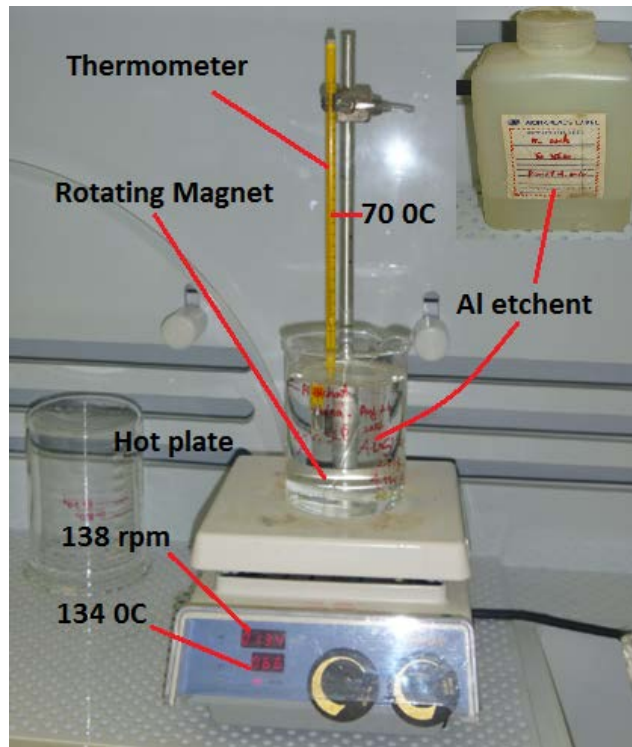


Figure 3.13. Apparatus for Al etching

Chart 3.6. Etchants for Insulators and Conductors (Paul 2005)

Material	Etchant Composition	Etch Rate
SiO ₂	28 ml HF 170 ml H ₂ O 113 g NH ₄ F	Buffered HF 100 nm/min
	15 ml HF 10 ml HNO ₃ 300 ml H ₂ O	
Si ₃ N ₄	Buffered HF H ₃ PO ₄	0.5 nm/min 10 nm/min
Al	1 ml HNO ₃ 4 ml CH ₃ COOH 4 ml H ₃ PO ₄ 1 ml H ₂ O	35 nm/min
Au	4 g KI 1 g I ₂ 40 ml H ₂ O	1 μm/min
Mo	5 mg H ₃ PO ₄ 2 ml HNO ₃ 4 ml CH ₃ COOH 150 ml H ₂ O	0.5 μm/min
Pt	1 ml HNO ₃ 7 ml HCl 8 ml H ₂ O	50 nm/min
W	34 g KH ₂ PO ₄ 13.4 g KOH 33 g K ₃ Fe(CN) ₆ H ₂ O to make 1 liter	160 nm/min

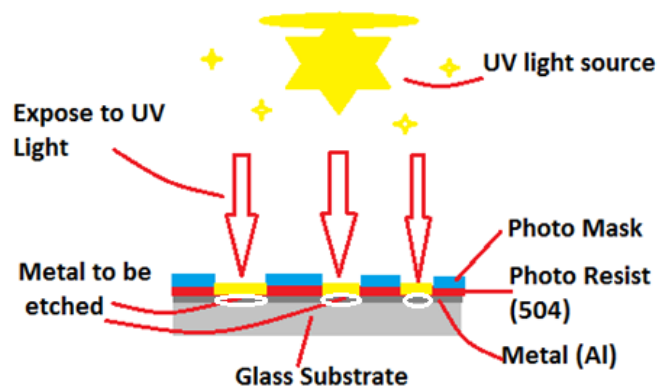
**Figure 3.14.** Preparation for wet (isotropic) etching



Figure 3.15. The patterned (etched) glass substrate view under optical microscope

3.6. Gas Chamber

The gas chamber planned to construct as first and second generation type. First generation type measurement taken according to flow measurement (sccm) second generation type to be construct to take measurement as parts per million (ppm). In this thesis all the gas flow measurement done according to first generation type. The chamber consisted of a stainless steel box with two ports for gas inlet and outlet. Gas flow controlled by valves and mass flow controller. Temperature and valve controlled by electronic controller that connected to the four valves. Voltage source, MFC and temperature + valve controllers connected to the gas chamber. The voltage source (Keithley Pico ammeter), mass flow controller and temperature + valve controllers are connected to computer integrated system. All the measurements observe, plot and saved by LabVIEW program. Gas chamber sample holder frame with a wide base was utilized to mount the substrate during testing and ensure uniform heat distribution. The chamber connected Argon, H₂ and CO₂ gases via MFC. We employed the gas chamber designed and implemented in the solid state physics laboratory at Ataturk University under the BAP project.

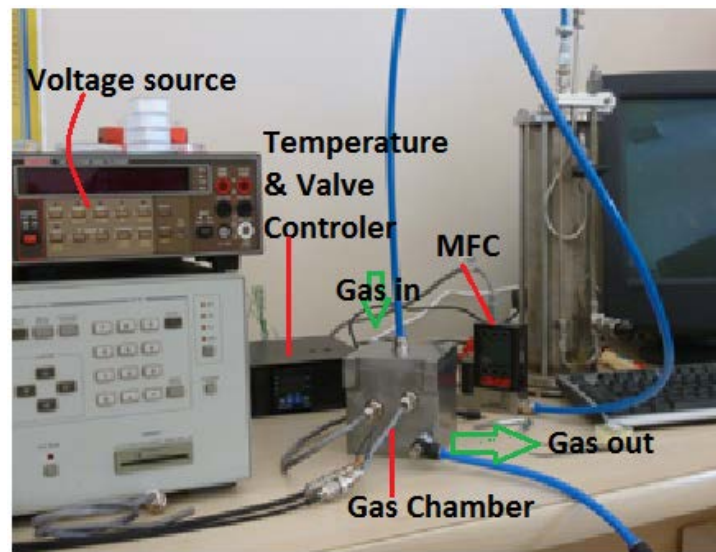


Figure 3.16. Gas chamber

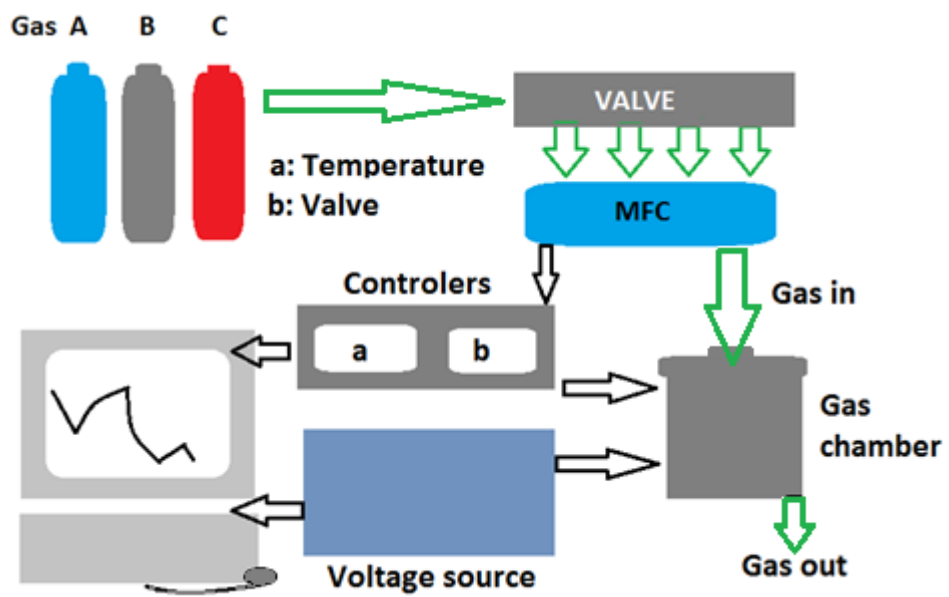


Figure 3.17. Schematic drawing of the gas delivery system

Gas Testing Procedure of this research, author tested the performance of the developed three types of ITO resistive sensors towards H_2 and CO_2 . Depending on the type of the sensor, each of them was tested at several operating room temperatures to elevated temperature (30°C, 50°C, 100°C, 150°C and 200°C). Integrated computer with LabVIEW program was utilized to automate the flow rate for the target gas with different concentrations the maximum 500 sccm. Initially, the inert/Argon gas maintained for 60/120 second accordingly. The sensors were exposed to Argon gas and observed stabilize the baseline. Only after the baseline gas was stable, the measurements were started by purging the sequences of the gas with different concentrations. Following parameters considered as an input parameters for measurements.

Chart 3.7. Input parameters for measurements

Input Parameters	Variable
Voltage source level (V)	0,30/0,50/1.0
Measurement gas set	400 sccm
Out gas set	400 sccm
Temperature (C)	30/50/100/150/ 200
Measurement time (s)	60/120/240
Out gas Time(s)	60/120/240
Measurement gas	Hydrogen (H_2)/ CO_2
Outer gas	Argon (Ar),

```

ITO3-2H2150C-60T - Not Defteri
Dosya Düzen Biçim Görünüm Yardım
V. source level = 0,10
Measu. gas set.:400,0
Out gas set.:400,0
Temperature: 150,0
Measu.Time(s):60
Out.gas Time(s):60
Measurement gas: Hydrogen(H2)
Outer gas: Argon(Ar)
Measu.gas valf:valf 4
Out gas valf:valf 2

11 Kas 2014 Sal 12:53:48-----
0.000 7801.890
0.125 7797.570
0.219 7797.570
0.344 7797.570
0.516 7797.570
0.703 7797.630
0.875 7797.690
1.047 7797.810
1.219 7791.190
1.391 7796.540
1.578 7796.540
1.750 7786.940
1.922 7786.940
2.094 7786.880
2.266 7779.130
2.453 7779.190
2.625 7782.220
2.797 7782.280
2.969 7775.200
3.141 7775.200
3.328 7770.310
3.500 7770.310
3.672 7777.500

```

Figure 3.18. Output of the sample gas sensing measurement dynamically and saved backup data using LabVIEW program

4. EXPERIMENTAL RESULTS and DISCUSSION

4.1. Characterization of ITO Thin films (XRD, SEM, EDAX and Absorption Techniques)

The surface morphology of the ITO thin films grown by sputtering in this thesis was observed by SEM (Scanning Electronic Microscope) QUANTA 450 FEG:FEI Company branded settled in Erzincan University and data of XRD (X-Ray Diffraction) were taken in a computer controlled diffractometer and with X-ray generator Cu K α radiation from an X-ray tube with normal focus X-ray diffraction (PANALYTICAL/Empyrean branded XRD in Erzincan University). Optical absorption/transmission measurements of the films measured in UV-visible-near infrared region by using a Perkin Elmer UV-VIS 2 Lambda spectrometer, which is available for wavelengths in the range of 200 nm to 1100 nm at Ataturk University.

Generally, XRD results shows that the thin films grown at different growth ambient are polycrystalline, except for the thin film grown without O₂ gas incorporation, despite depositing them at room temperature, without post-heat treatment. Figure 4.1-4.3 shows X-ray diffraction patterns of ITO films grown by RF magnetron sputtering as a function of oxygen partial pressure in the sputtering ambient. In order to confirm the repeatability of the characteristics of the grown samples, two thin films were grown at the same growth condition at two different times. Figure 4.3 shows the XRD data obtained for these samples and it shows almost similar XRD result confirming the repeatability of the thin films. The preferential orientation of the ITO films depends on the oxygen partial pressure as shown in Figure 4.1- 4.3 an ITO film grown with no O₂ incorporation during the growth shows a different XRD results. As shown in Figure 4.1 (a), there is no clear narrow diffraction peak corresponding to any particular planes. This can be attributed to the O₂ incorporation during the growth helps the formation of the ITO films.

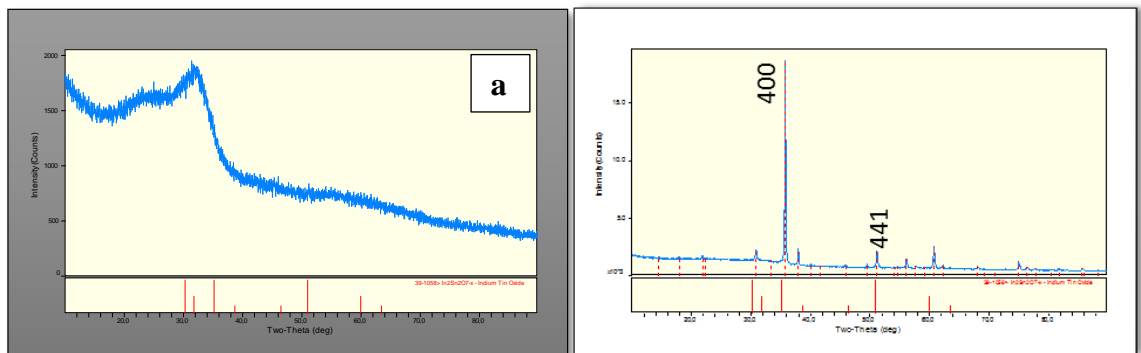


Figure 4.1. XRD results of the thin films grown at O_2 partial pressure at a) $P(O_2)=0\%$ (pure ITO, Device 5) b) $P(O_2)=2.7\%$

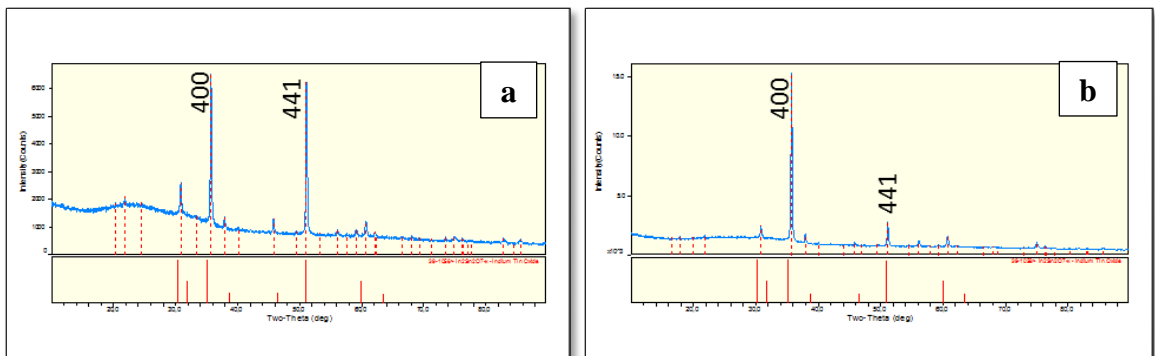


Figure 4.2. XRD results of the thin films grown at O_2 partial pressure at a) $P(O_2) = 13.5\%$ (Device 4), b) $PO_2 = 16.3\%$ (Device 3)

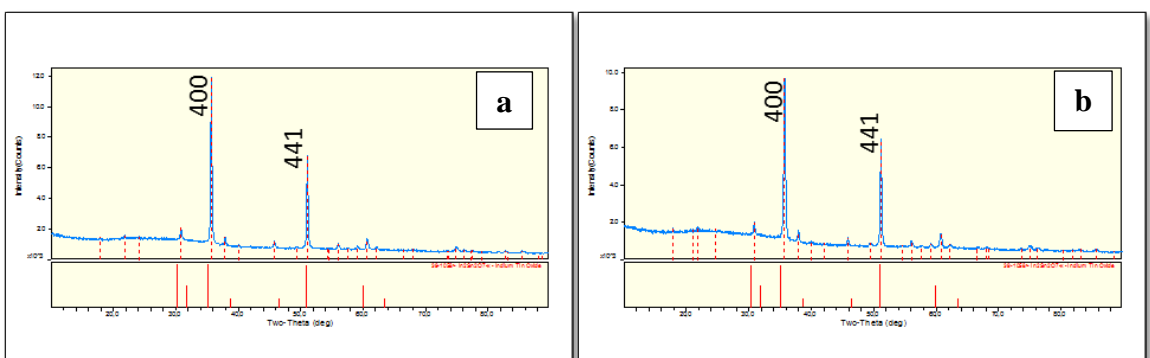


Figure 4.3. XRD results of the thin films grown at O_2 partial pressure at a) $P(O_2) = 11.74\%$ b) $P(O_2) = 11.74\%$

Figure 4.4. Shows how percentage of the O_2 partial pressure effects on the XRD patterns of the grown thin films. As it can be seen clearly, for lower O_2 partial pressures

thin films show a preferential (400) plane orientation parallel to the substrate surface. On the other hand, dominance of (400) plane decreases and (441) plane increases when the O₂ partial pressure increases. The result decreasing diffraction intensity of the (400) peak as the increasing oxygen partial pressure was also observed in literature (Kim *et al.* 2009).

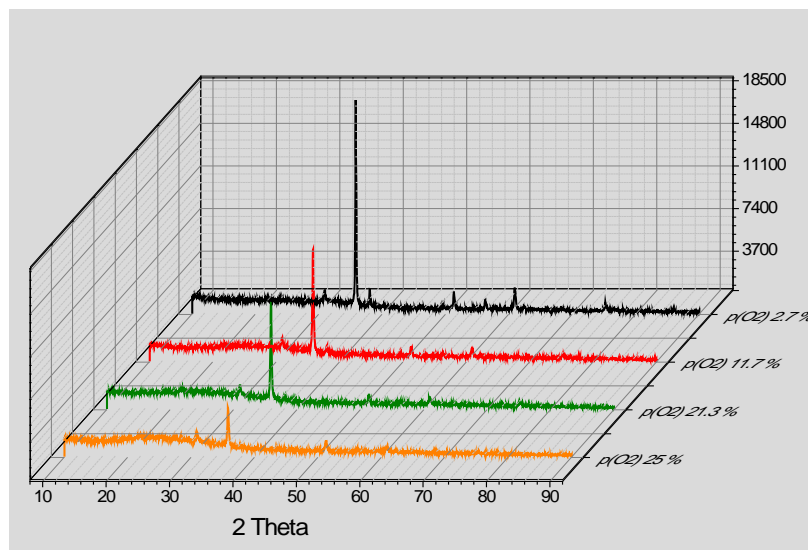


Figure 4.4. Shows increase of O₂ partial pressure decrease the crystallinity of the thin films

Some parameters calculated from the XRD measurements are tabulated as shown in Chart 4.1. Figures 4.1 to 4.3 and Chart 4.1 predict dominant crystal phase as (400) when O₂ ratio is low. Peak belongs to (400) height decreased and (441) peak started to increase as the O₂ partial pressure increases. Grains sizes calculated from the Scherrer's formula as given in equation 4.1. Obtain grain sizes are between 39.4 nm to 62.8 nm.

Scherrer's formula:

$$D = \frac{(K \lambda)}{(\beta \cos \theta)} \quad (4.1)$$

D is mean grain size, $K=0.9$, the diffractometer used is with $\text{CuK}\alpha$ radiation so $\lambda=1,5406\text{\AA}$, β is the full width at half of the peak maximum (FWHM) in radians and Θ is Bragg's angle.

Chart 4.1. Summary of the XRD results and calculation

S/D:no	O ₂ %	T (nm)	2 θ (400)	I% (400)	FWHM (400)	D (nm)	2 θ (441)	I% (441)	FWHM (441)
Pure/(5)	0	333	-	-	-	-	-	-	-
3	2.7	983	35.8	100	0.13	62.8	51.3	8.61	0.17
9	11.7	250	35.8	100	0.30	27.8	51.24	82.6	0.20
12/(4)	13.5	335	35.8	83.9	0.19	56.5	51.2	100	0.16
11/(3)	16.3	825	35.7	100	0.11	76.6	51.1	15.6	0.17
4	25	402	35.8	100	0.21	39.4	51.2	29.4	0.23

G.R: Growth Rate, D: Grain Size, I: Intensity t: thickness, S/D: Sample/Device

SEM images for the ITO films shown in Figure 4.6 through 4.8. From SEM image, the film deposited without oxygen addition during sputtering is composed of compacted nano-size grains (nucleation) (Figure 4.5 (a) and EDAX measurement predicts that the absence of Sn into the structure which confirms the formation of In_2O_3 . However, at 2.7% oxygen pressure, film is ITO according to EDAX results through SEM analysis, grains are rod-like structured as shown in Figure 4.5 (b). Film composition determined from EDAX results is $\text{In}_{1.66}\text{Sn}_{0.34}\text{O}_{6.55}$.

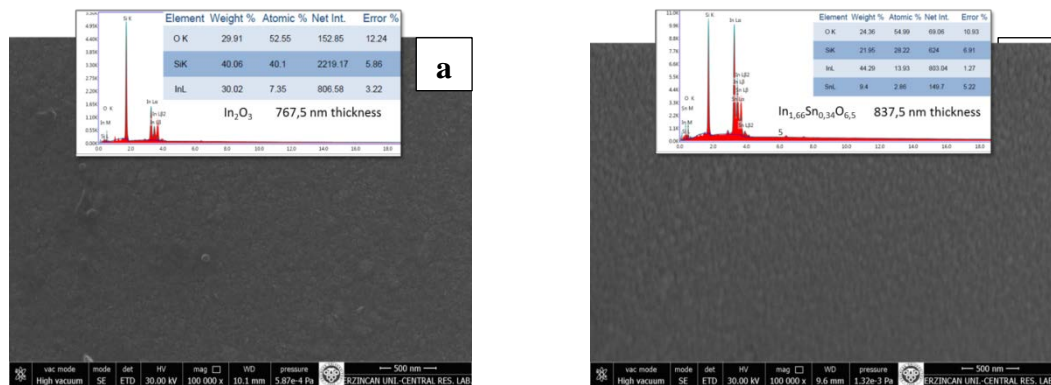


Figure 4.5. a) SEM and EDAX images for P (O_2)= 0% (pure ITO-Device 5) b) P (O_2)=2.7%

The SEM investigation of RF sputtered layers reveals a significant difference as a function of the sputtering conditions. The surface of these samples seems to be formed by small nano-sized grains. In our study the parameters results for RF sputtering at room temperature are significantly better than those reported in the literature for similar processes (Yoo *et al.* 2004). SEM images of pure ITO sample (Figure 4.6) shows smaller grains than the thin film grown at 2.7% 13.5% and 16.3% O₂. Film deposited under 11.7% O₂ pressure has the biggest grain sizes formed as shown in Figure 4.7. EDAX result for this thin film predicts In_{1.84}Sn_{0.16}O_{5.85}.

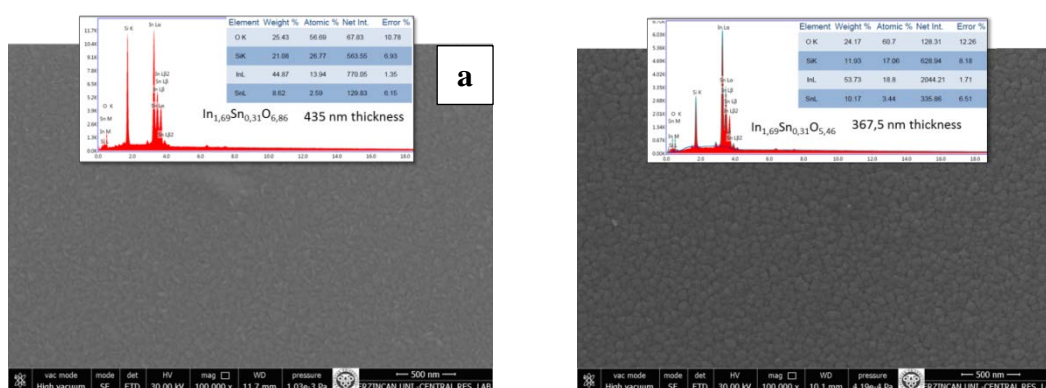


Figure 4.6. a) P(O₂)=13.5% (Device 4) b) P(O₂)=16.3% (Device 3)

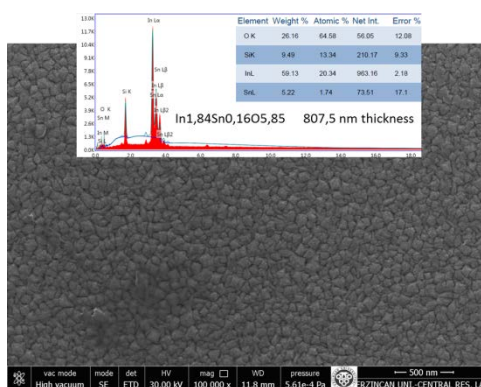


Figure 4.7. SEM and EDAX images for P(O₂)=11.7%

As Yamazoe 2003 states that gas sensors utilize porous polycrystalline resistors made of semiconducting oxides. The working principle involves the receptor function played by

the surface of each oxide grain and the transducer function played by each grain boundary. Therefore we attempt to compare sensing performance with SEM and XRD results.

Chart 4.2 shows the calculation of the resistivity, growth rate of the thin films grown at different O₂ partial pressure ambient. The thicknesses of the films were measured by using a Alfa step profilometer with scanning length 5000 μm scanning direction → and range 13μm/1Å.

Chart 4.2. Summarized chamber conditions and FPP results.

Sample no	Time	O ₂ %	Sheet Resistance SQ-cm	Thickness cm	Resistivity Ω – cm	Growth rate nm/min
1	15	21.3	1.925x10 ⁴	8.86x10 ⁻⁵	1.70	-
2	15	11.7	1.025x10 ⁵	2.5 x10 ⁻⁵	2.56	44.2
3	15	2.7	1.182x10 ⁵	9.83x10 ⁻⁵	11.6	55.8
4	15	25.0	-	3.63x10 ⁻⁵	-	26.8
5	20	16.3	1.543x10 ⁵	9.0x10 ⁻⁵	13.9	55.0
6	20	13.5	2.39x10 ⁵	1.38x10 ⁻⁵	8.57	50.7
7	15	9.6	1.632x10 ⁵	2.58x10 ⁻⁵	4.2	-
8	15	6.9	3.18x10 ⁵	5.43x10 ⁻⁵	17.3	-
9	15	11.7	2.06x10 ⁵	6.63x10 ⁻⁵	13.7	44.2
10	15	11.7	3.8x10 ⁵	1.00x10 ⁻⁴	38.7	44.2
11	15	16.3	7.34x10 ⁴	8.25x10 ⁻⁵	6.06	55.0
Pure	5	0.0	-	3.33x10 ⁻⁵	-	66.6

Figure 4.8 shows the growth rate change obtained from the thickness/growth time with the O₂ partial pressures. As shown from the Figure 4.5, there is a general trend which is decreasing growth rate by increasing O₂ partial pressure. Also, Figure 4.9 shows the variation of the resistivity of the thin film versus O₂ partial pressures. As shown from the Figure 4.9 that the increasing O₂ partial pressure causes to decrease in the resistivity values.

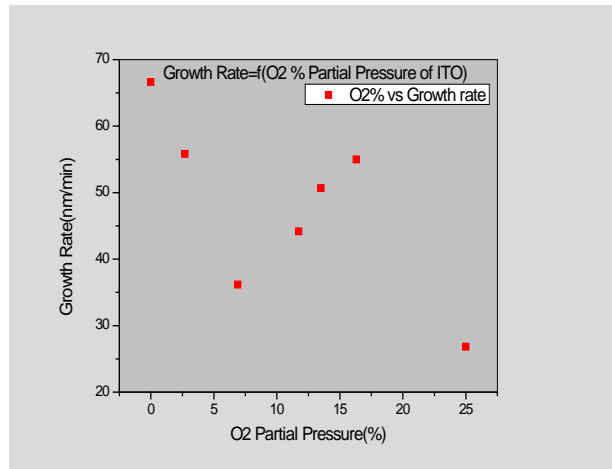


Figure 4.8. Growth rate vs O₂ partial pressure variation

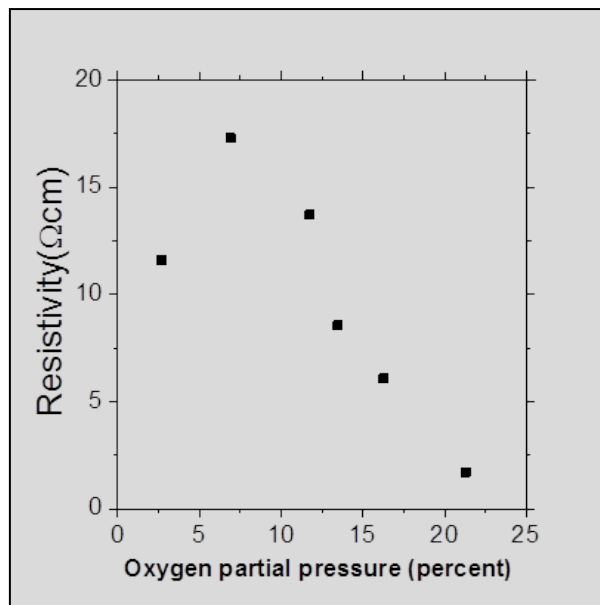


Figure 4.9. Resistivity vs O₂ partial pressure variation

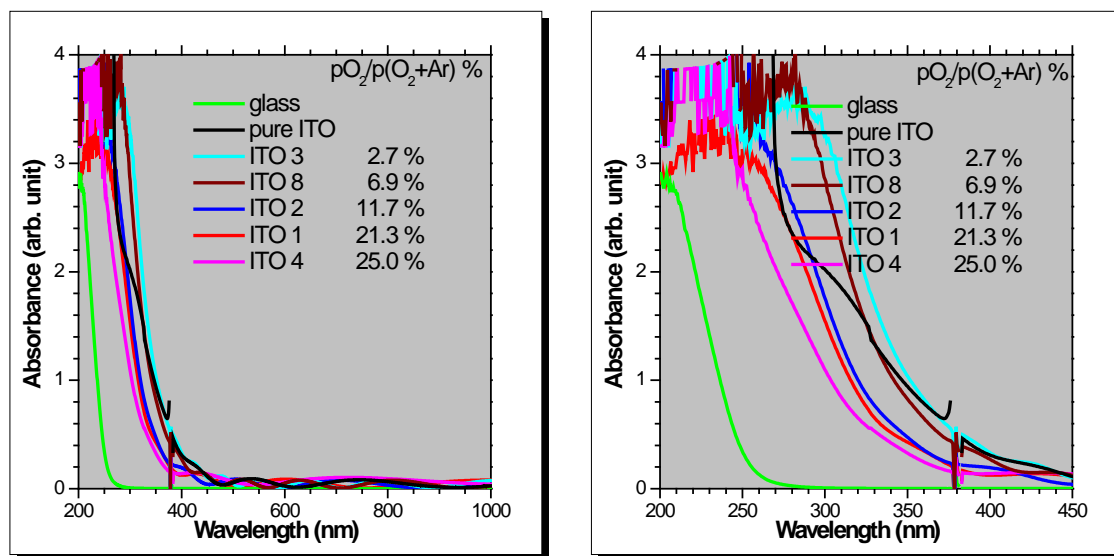


Figure 4.10. Absorption measurements of the ITO thin films a) 200-1000 nm b) 200-450 nm

Figure 4.10 (a) and (b) shows absorption measurements of ITO thin films grown at different O_2 partial pressures. As shown from the Figure 4.10 above that the change in the O_2 partial pressure causes to shift in the absorption spectrum of the ITO thin films. This means that the increasing partial pressures of the O_2 causes to change in the bandgap value of the ITO films. Absorption measurements were taken reference to the glass substrate and the absorption spectrum of the glass sample has shown to confirm the observed absorptions due to the grown thin films. As shown the glass shows absorption spectra which start to increase at around 250 nm, while the ITO films show the absorption spectra increase between 350-400 nm.

Figure 4.11 to 4.16 shows the absorption coefficient versus incoming light energy variation of the samples and the calculations of the bandgap from the square of the absorption coefficient. The figures from 4.11 to 4.16 are plotted graphs of absorption coefficient vs energy and square of absorption coefficient vs energy are drawn using originPro 8.5 software. Figure 4.11 (a) absorption coefficient and (b) Square of absorption coefficient vs energy graph for pure ITO (0% O_2) shows the fit to find the bandgap value of the thin film. As shown from the figure 4.11 (b) two fits can be seen

in lower energy side and higher energy side of the plot. With respect to figure 4.5 (a) compositional analysis of ITO thin film comparing EDAX results with band gap values shows this can be because In_2O_3 band gap. While lower energy side In_2O_3 and higher energy side assumed as ITO. Therefore between ITO and In_2O_3 brings us phase separation. EDAX result confirmed In_2O_3 formation to bandgap of $\text{In}_2\text{O}_3=3.46$ eV. These graphs drawn according to the increment of O_2 partial pressure. Later calculated bandgap tabulated in Chart 4.3 descending order.

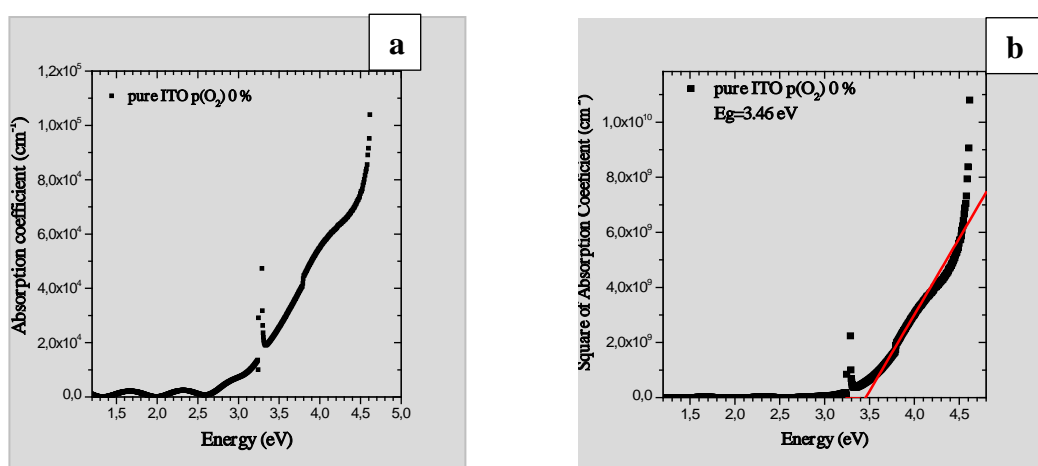


Figure 4.11 a) Absorption coefficient and **b)** Square absorption coefficient vs energy graph for pure ITO

Figure 4.11 (b) graph shows red line - fit made on the plot to calculate bandgap. The band gap for pure ITO 0% O_2 was $E_g=3.46$ eV obtained.

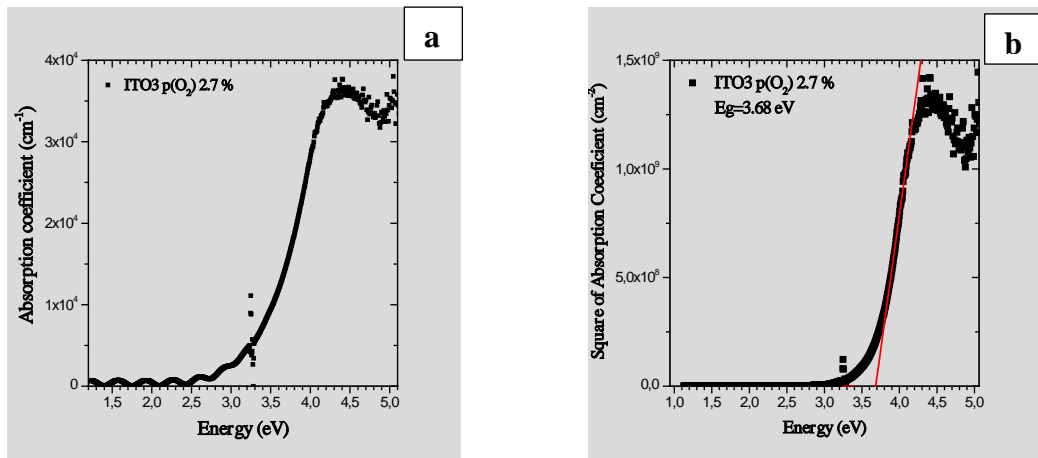


Figure 4.12. a. Absorption coefficient and **b.** Square absorption coefficient vs energy graph for (2.7% O₂)

Figure 4.12 (b) graph shows red line - fit made on the plot to calculate bandgap. The band gap for pure ITO 2.7% O₂ was Eg=3.68 eV obtained.

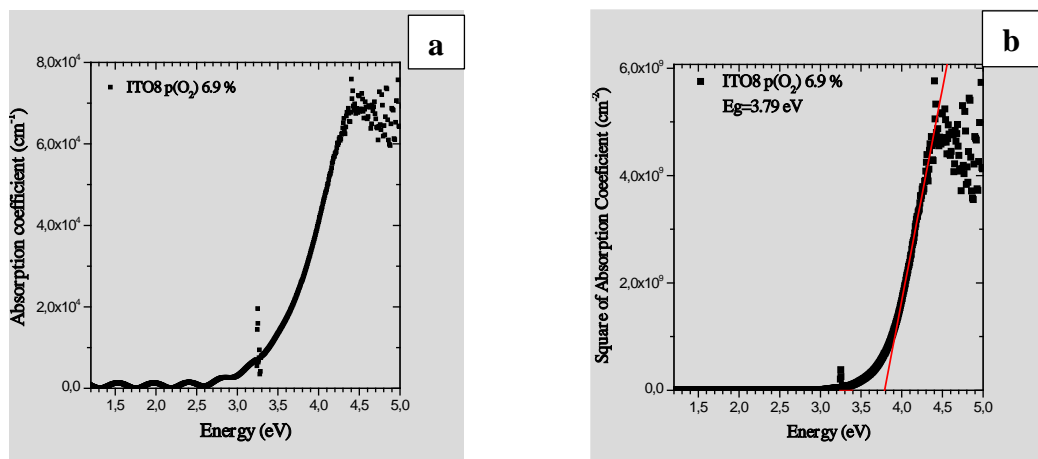


Figure 4.13. a. Absorption coefficient and **b.** Square absorption coefficient vs energy graph for (6.9% O₂)

Figure 4.13 (b) graph shows red line-fit made on the plot to calculate bandgap. The band gap for pure ITO 6.9% O₂ was Eg=3.79 eV obtained.

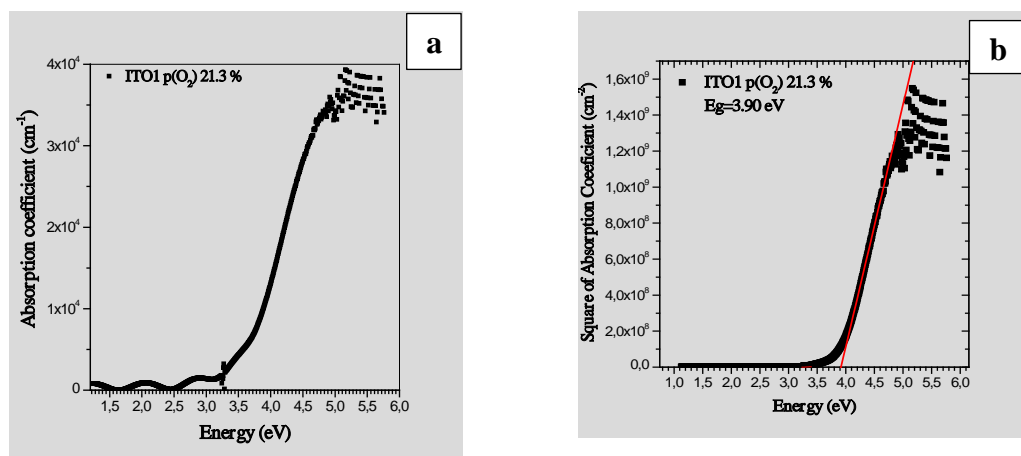


Figure 4.14. a. Absorption coefficient and **b.** Square absorption coefficient vs energy graph for (21.3% O₂)

Figure 4.14 (b) graph shows red line - fit made on the plot to calculate bandgap. The band gap for pure ITO 21.3% O₂ was Eg=3.90 eV obtained.

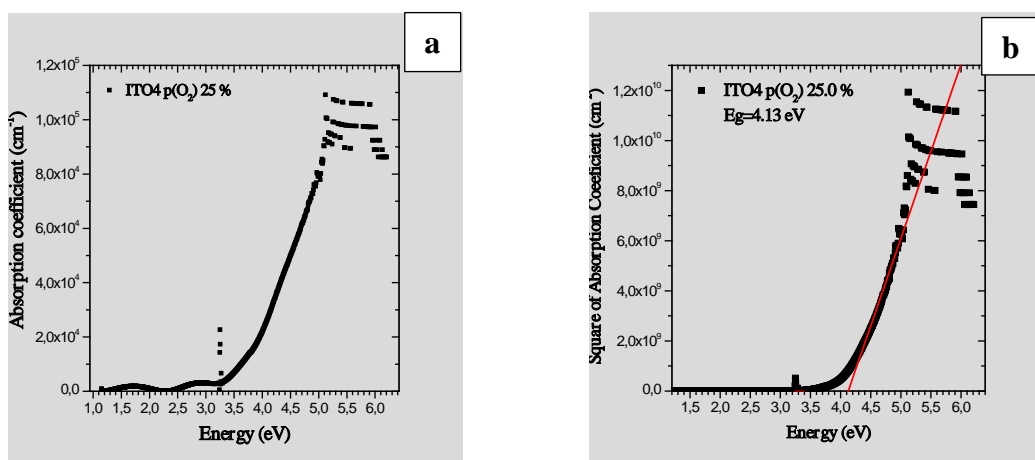


Figure 4.15. a. Absorption coefficient and **b.** Square absorption coefficient vs energy graph for (25% O₂)

Figure 4.15 (b) graph shows red line - fit made on the plot to calculate bandgap. The band gap for pure ITO 25% O₂ was Eg=4.13 eV obtained.

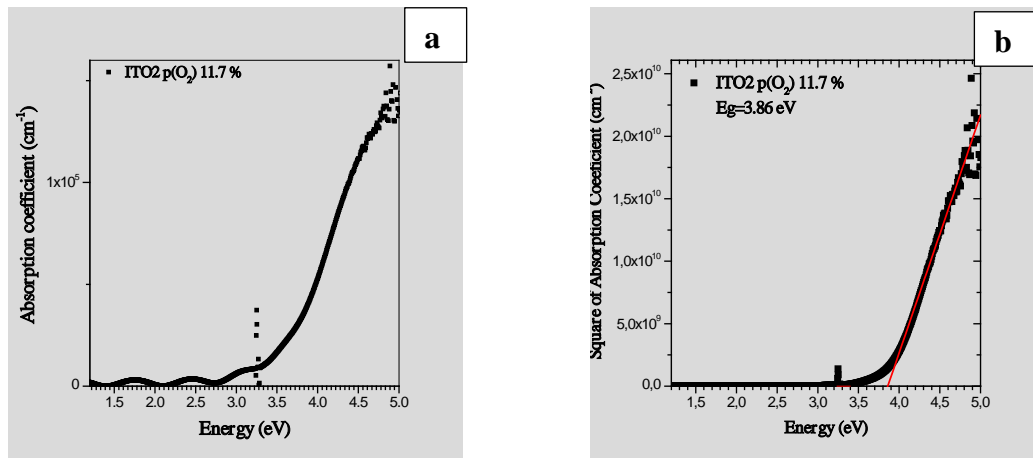


Figure 4.16. a. Absorption coefficient and **b.** Square absorption coefficient vs energy graph for (11.7 % O₂)

Figure 4.16 (b) graph shows red line - fit made on the plot to calculate bandgap. The band gap for pure ITO 11.7% O₂ was E_g=3.86 eV obtained.

The band gap calculations for Figure 4.11 to 4.16 are concluded in the Chart 4.3. shows that bandgap increasing with respect to O₂ partial pressure.

Chart 4.3. Bandgap Variation

P(O ₂) %	Bandgap	Reflection coefficient (%)
Pure	3.46	0.54
2.7	3.68	0.35
6.9	3.79	0.3
11.7	3.86	0.2
21.3	3.9	0.36
25.0	4.13	1.9

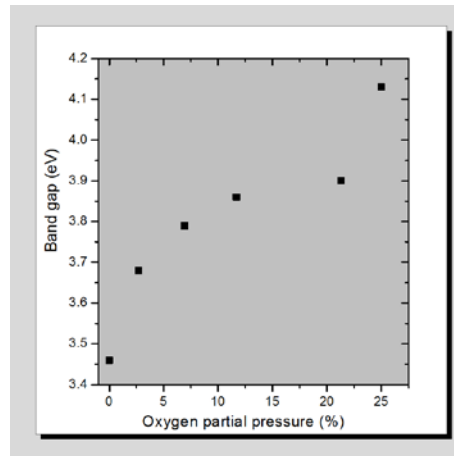


Figure 4.17. Bandgap variation with reference to the O_2 partial pressure

Chart 4.3 and Figure 4.17 shows bandgap increase with increase of O_2 partial pressure. So Figure 4.17 plot predicts bandgap go higher with respect to O_2 partial pressure.

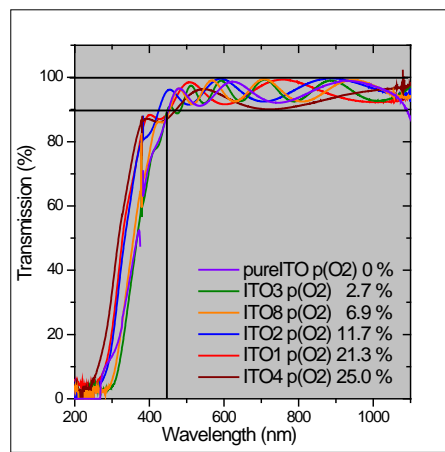


Figure 4.18. The figure shows very high transmittance of the grown ITO films

Figure 4.18 shows the transmission versus wavelength plots for the ITO thin films varying to O_2 growth ratio in the growth ambient. As shown from the figure that the transmittance of the thin films are above 90% between 420 nm-1100 nm which is very good compared to the literature (Chen *et al.* 2013). According to the Figure 4.18 and

calculated results from formula 2.4 and 2.5 shows ITO thin film shows high transparency and relatively high resistivity compared to the literature.

Transparency values summarized in Chart 4.4 values obtained within 420nm–1100nm F.O.M is a parameter generally used to characterized performance of ITO. We obtained the order of 10^{-5} for our results.

Chart 4.4. Figure of Merit (FOM) of ITO thin films

P(O ₂) %	Transparency	Sheet Resistance SQ-cm	Resistivity Ωcm	FOM
Pure	0.91	-	-	-
2.7	0.92	1.18×10^5	11.6	0.37×10^{-5}
6.9	0.92	3.18×10^5	17.3	0.14×10^{-5}
11.7	0.92	3.80×10^5	38.7	0.11×10^{-5}
21.3	0.92	1.93×10^4	1.7	0.22×10^{-4}
25.0	0.90	-	-	-

4.2. Gas sensor characterization and measurements

In this ITO gas sensor device fabrication process we developed three hypotheses to explain sensitivity.

1. Research on how the characteristics of the ITO films change when O₂ partial pressure increase / decrease during the growth.
2. Research on how influence O₂ partial pressure to improve the sensitivity for different gas specious.
3. Research how geometry and surface volume ratio impact on sensitivity of ITO based gas sensors.

However in this experiment we shall prove and explain first and second hypothesis. The main goals of this work were to develop and compare the performance of the ITO gas sensing devices. We deposited ITO thin films and fabricated several devices that have different patterns, different sizes and different O₂ ratios. The measurements performed concerned for 16.3% O₂, 13.5% O₂ and 0% O₂ devices only. The sensors produced based on chemo-resistive type with ITO wide bandgaps and thin film sensing layer formed upper. The bottom glass substrate patterned by Al interdigitate thin film contacts. Above mentioned three devices differs each other according to sputter chamber conditions that we provided.

All three types of devices (16.3% O₂, 13.5% O₂ and 0% O₂) under 30°C, 50°C, 100°C, 150°C, and 200°C elevated temperature individually to measure the resistance change in gas vicinity while time as variable. In this discussion we account only lower temperature 30°C and highest temperature 200°C that we measured. All the sensing performance observed dynamically and saved backup data using LabVIEW program. We found satisfactory and promising results from the ITO sensors for H₂ and CO₂ gases. These sensors showed different performance for both types of gases.

Hydrogen gas showed highest sensitivity for 0% O₂ device. By examine the data we found Ar/O₂ ratio shows significant impact on gas sensitivity. Same time absorption results shows band gap variation according to the chamber condition provided to fabricate sensor. The SEM images show grain size variation for different chamber conditions. The XRD characterization was good evidence for to prove the thin film having good oriented crystal structure. We raised here some references from previous scientific research to show our results and SEM, XRD characterization having good agreement with those. Importantly absorption measurement showed how bandgap and figure of merits changes while changing partial pressure.

As a first step declared if interdigitate back contacts shows ohmic behavior allowing to the measuring gas sensing behavior. Before every measurement, contacts' ohmic behavior was confirmed by I-V measurements. We obtained resistance vs time graph for

the every single measurements with temperature as a variable. Responsivity for the ITO gas sensors calculated according to fractional method as explained below. As simply, the baseline is subtracted from the response $X_s(t)$ and then divided by the baseline $X_s(0)$ from the sensor response which provides a dimensionless, normalized response $Y_s(t)$ that can compensate for inherently large or small signals.

$$\text{Responsivity \% } Y_s(t) = \frac{X_s(t) - X_s(0)}{X_s(0)} \times 100 \quad (4.2)$$

In this experiment, response time and recovery time measurements obtained according to step response of first order sensor response (Webster *et al.* 1999). Prior to our result and discussion we conclude some scientific work that shows responsivity, response time and recovery time towards to H_2 and CO_2 gases

Since the sensitivity (S), selectivity (SE), response time t_{res} , recovery time t_{rec} , and the range of operating temperature for the optimum detection T_{opt} are the most important parameters that decide which sensor is better than the others we have arranged our results in Charts to enable an easy comparison. Initially the sensors were tested for the response to H_2 and CO_2 gas with fixed 400 sccm for different temperatures, starting from 30°C to 200°C Graph 4.1 to 4.11 presents the resistance variation versus time as a function of the successive increase temperature. The resistance of ITO thin films increases or decreases after exposure to the oxidizing or reducing gas species (CO_2/H_2) and it returns to the initial value when the CO_2/H_2 gas is removed (Hagen, W. *et al.* 1983).

Following the procedure explained in Chapter 3.6 of gas sensor measurements we summarized the measurement results for gas sensor devices for 0% O_2 , 13.5% O_2 and 16.3% O_2 . Figure 4.19 - 4.20 show CO_2 and H_2 gas response measurements of the 16.3% O_2 device, respectively. As shown in the figures in H_2 gases we observed responsivity 1% at 30°C while for the CO_2 response is not observed, at elevated temperature 200°C the measurement shows a significant response. Chart 4.5 shows the

responsivity analysis of the 16.3% O₂ device almost equal for both H₂ and CO₂ gases. As shown in the Chart 4.5, 9.2% responsivity is obtained for CO₂ and 10.9% responsivity for H₂ gases obtained. The response and recovery time obtained for the H₂ gas is 39.8, 62.1 seconds respectively. For CO₂ gases response and recovery time is 32.8, 36.4 seconds respectively. We can see for CO₂ took twice longer time but H₂ response time and recovery time almost equal at 200°C.

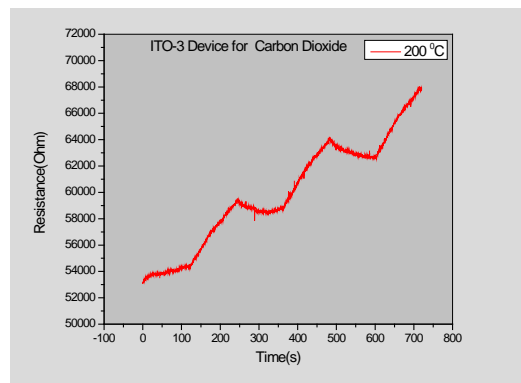


Figure 4.19. ITO 3 (16.3% O₂) Device CO₂ at 200°C

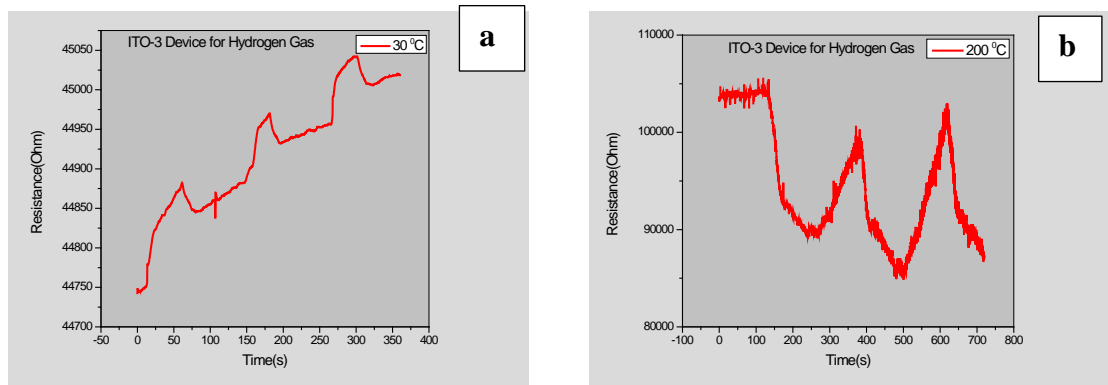


Figure 4.20. ITO3 (16.3% O₂), **a.** H₂ at 30°C, **b.** H₂ at 200°C

The Chart 3.4 shows the growth conditions of the grown ITO devices. ITO3, ITO4 and ITO5 (16.3% O₂, 13.5% O₂ and 0% O₂) devices were measured and O₂ effect during the growth was investigated on the performance of the devices.

Chart 4.5. Comparison of ITO 3 (16.3% O₂)

ITO3	Responsivity %		Response Time (seconds)		Recovery Time (seconds)	
	30°C	200°C	30°C	200°C	30°C	200°C
CO ₂	-	9.2	-	39.8	-	62.1
H ₂	0.08	10.9	-	92.3	-	36.4

As shown in the figure 4.21– 4.22 and Chart 4.6 shows, for H₂ and CO₂ gases we could not get proper responsivity at 30°C, at elevated temperature 200°C the measurement shows favorable response. The analyzed responsivity of the ITO 4 (13.5% O₂) device for H₂ slight higher than CO₂ gases. As shown in the Chart 4.6, 6% responsivity is obtained for CO₂, 9.8 % obtained for H₂. The response time and recovery time obtained for the H₂ gas is 10.5, 28.7 seconds respectively and for CO₂ gases response time and recovery time is 28.7, 4.4 seconds respectively. We can see for CO₂ took three times longer for recover other hand H₂ 1/6th time faster recovered at 200°C

Chart 4.6. Comparison of ITO 4 (13.5% O₂)

ITO4	Resistivity %		Response Time (seconds)		Recovery Time (seconds)	
	30°C	200° C	30°C	200°C	30°C	200°C
CO ₂	-	6.0	-	10.5	-	28.7
H ₂	-	9.8	-	23.6	-	4.4

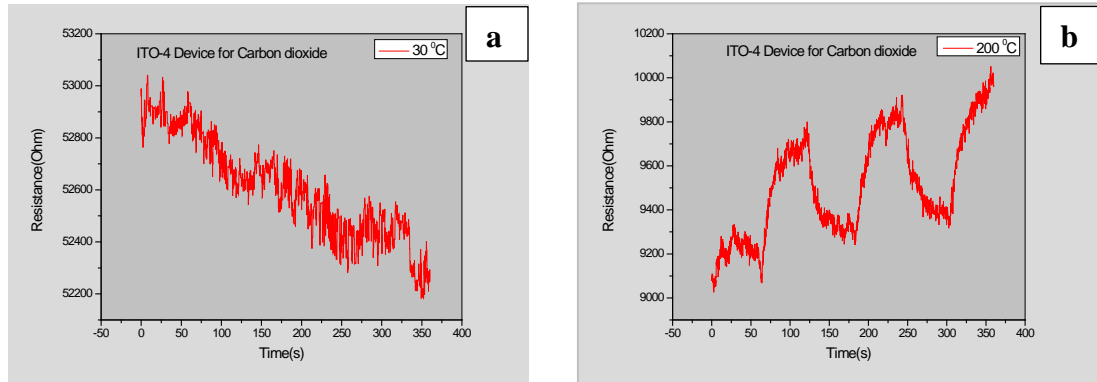


Figure 4.21. ITO4 (13.5% O₂) **a.** CO₂ at 30°C, **b.** CO₂ at 200°C

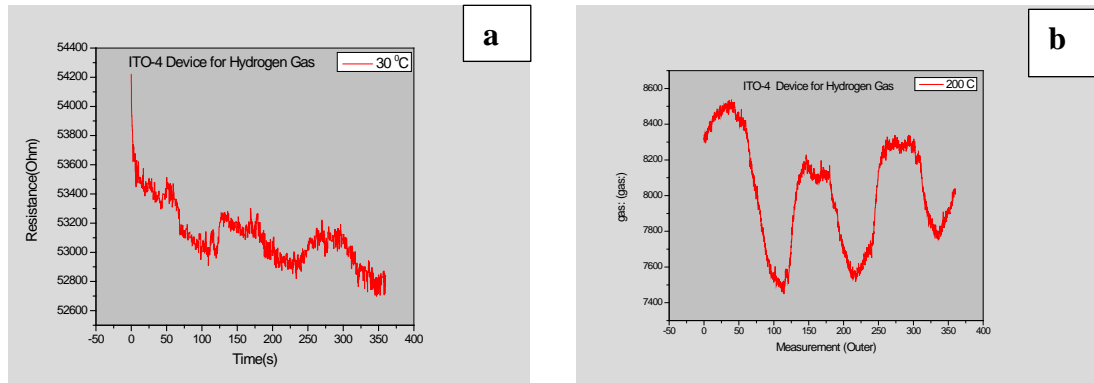


Figure 4. 22. ITO4 (13.5% O₂) **a.** H₂ at 30°C, **b.** H₂ at 200°C

Figure 4.23- 4.26 and Chart 4.7 shows that CO₂ and H₂ gas response measurements of the ITO5 (0% O₂) device, respectively. As shown in the figures in H₂ gases we observed responsivity 22% at 200°C while for the CO₂ response was observed 4%, at elevated temperature 200°C the measurement shows a significant response. Chart 4.7 the analysis responsivity of the ITO5 (0% O₂) device H₂ shows 5 times higher than CO₂ gases. The response and recovery time obtained for the H₂ gas is 92.3, 24.2 seconds respectively. For CO₂ gases response and recovery time is 68.1, 105.8 seconds respectively. We got interesting result for ITO 5 (0% O₂) measurements. CO₂ took one and half time longer than response time to recover while H₂ recovered 4 times faster than response time. That shows us ITO 5(0% O₂) obeyed closer to theoretical numbers

we find in literature (Webster 1999). As both gases reaction opposite to each other this sensor can be candidate for selectivity over CO₂ gas.

Chart 4.7. Comparison of ITO 5 (0% O₂)

ITO5	Resistivity		Response Time		Recovery Time	
	%		(seconds)		(seconds)	
	30°C	200°C	30°C	200°C	30° C	200°C
CO ₂	-	4.1	-	68.1	-	105.8
H ₂	-	22	-	92.3	-	24.2

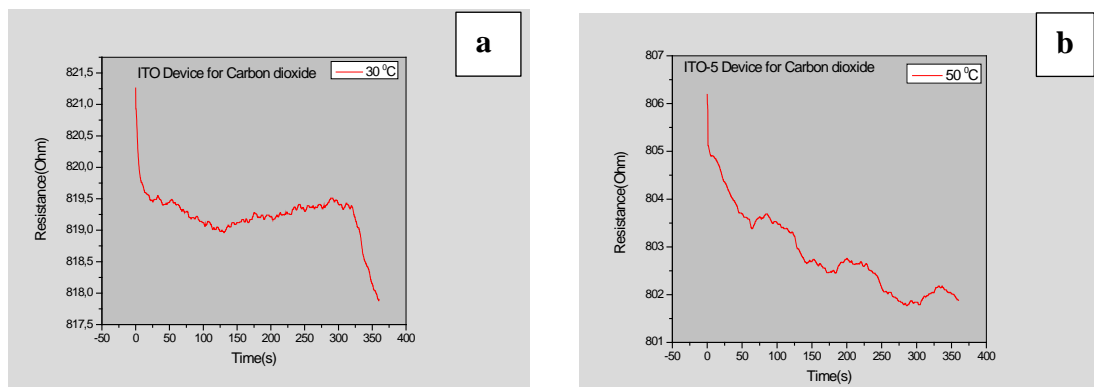


Figure 4.23. ITO5 **a.** CO₂ at 30°C, **b.** CO₂ at 50°C

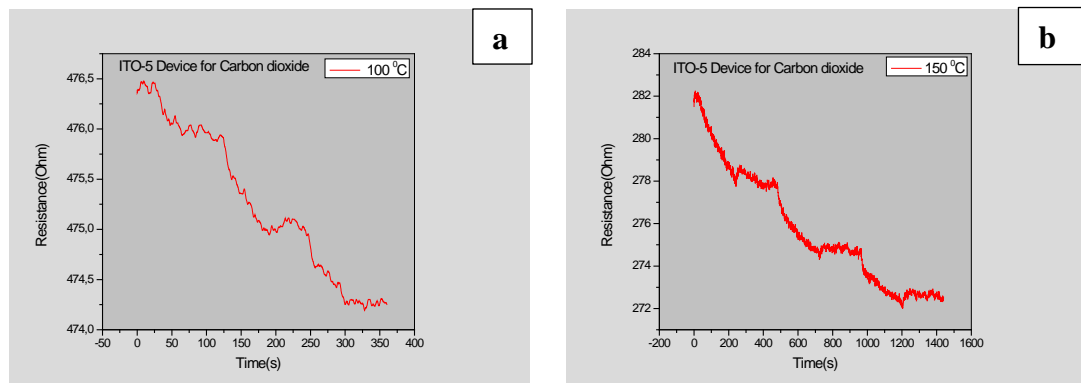


Figure 4.24. ITO5 **a.** CO₂ at 100°C, **b.** CO₂ at 150°C

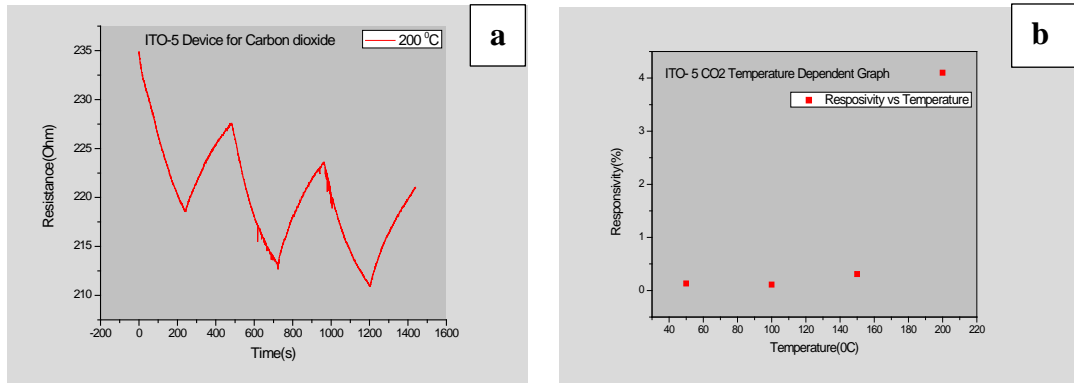


Figure 4.25. ITO5 a CO₂ 30 °C., b. CO₂ at 200°C, Temperature vs Responsivity

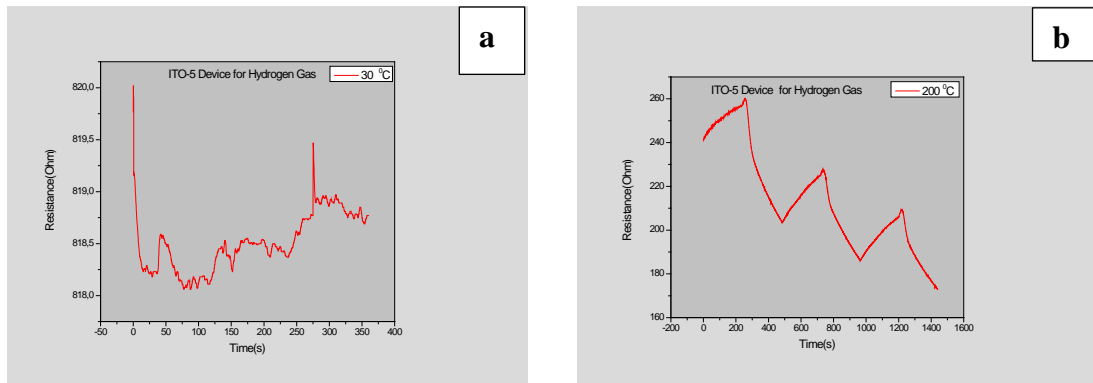


Figure 4.26. ITO5 a. H₂ at 30°C, b. H₂ at 200°C

Chart 4.8. Comparison of ITO 5 (0% O₂) for CO₂ Temperature dependency

ITO5	Sensitivity%					Response Time (seconds)		Recovery (seconds)	
	30°C	50°C	100°C	150°C	200°C	30°C	200°C	30°C	200°C
CO ₂	-	0.13	0.11	0.31	4.1	-	68.1	-	105.8

Figure 4.23–4.25 plots and Chart 4.8 predicts CO₂ sensitivity for 30°C to 200°C elevated temperatures. This variation shows how gas responsivity depending on up rise the temperature.

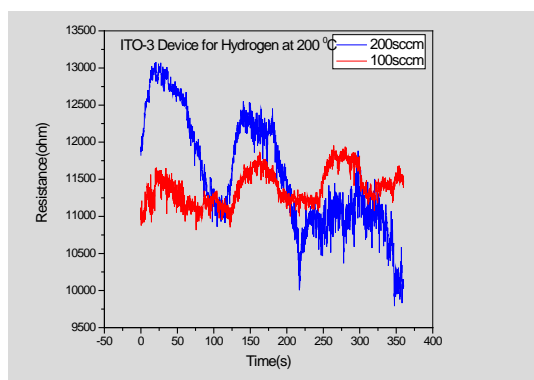


Figure 4.27. Changing the resistance on different Gas Concentration (sccm)

Figure 4.27 is a good illustration for different concentrations having an impact on resistance change. It shows how higher/lower the sccm affects the change of resistance. Shown for 100 and 200 sccm under 200°C temperature.

An electronegative molecule such as CO_2 is approaching the semiconductor surface and its electron affinity χ is larger than the semiconductor work function Φ_s , the molecule will tend to pick up an electron from the semiconductor conduction band and become chemisorbed at the surface. The net result of the chemisorption of the acceptor-type gas such as CO_2 on an n-type semiconductor surface is a decrease in electron concentration in the conduction band near the semiconductor surface, and hence a decrease in the conductance close to the surface (Majdeddin 2006). We observed such changes in our measurements.

The variations of normalized resistances at five different operation temperatures for 400 sccm H_2 and CO_2 exposure is shown in Figures. At low operating temperature, the sensor responded slowly and higher operating temperature caused a faster response. At the same time, if the temperature is higher, the interaction will be stronger. Therefore, the recovery time becomes longer at higher operation temperatures. In particular, as the operating temperature increases from room temperature to 200°C, the response time decreases from 8.6 s to 92.3 s but the recovery time increases from 7.7 s to 105.8 s as shown in Figures shows for CO_2 vice-versa 19.1 s to 92.3 s and 2.6 s to 24.2 s for H_2 gas

for ITO device 5. This device showed us equal to theoretical resistive sensor results as response time should be equal to $1-1/e$ and recovery time equal to $1/e$ (Webster 1999)

In this work we have defined the response time as the time required for the sample resistance to reach 63.2% ($1-1/e$) of the equilibrium value, while we define the recovery time as the time necessary for the sample to return to 36.8% ($1/e$). We provided the response and recovery of ITO thin films upon varying 100, 200, 400 sccm flow rate 200°C . The response (recovery) was found to become faster (slower) with increasing sccm. But the film resistance can return to exactly its initial value after a few seconds. Taking into account the response amplitude and the response, as well as the recovery times, the experimental results indicate that the optimal operating temperature of the sensor for CO_2 and H_2 is 200°C . Temperature is a very important parameter of the sensor because, if it is different for various gaseous species, it can be related to the selectivity. When it is in a low range of values it offers the possibility to perform a sensor with a low cost of energy consumption. Above graphs shows the dependence of response R and the sensitivity S on the 400 sccm at different operating temperatures. We have found that the response to CO_2 increases non-linearly with increasing temperature H_2 decreasing. vise-versa. The non-linear response to increasing temperature of oxidizing gases may be due to the filling of adsorption sites on the ITO surface, which proportionally decrease as the concentrations increase. This dependence of the sensitivity (S) on partial pressures of CO_2 follows the well-known power law for metal-oxide semiconductor sensing films, If we are interested in the determination of high sccm rates, we can operate the sensor at higher $^{\circ}\text{C}$, since the slope is higher. Otherwise, if we are interested in lower sccm rates, we should work at lower $^{\circ}\text{C}$ because at this temperature the detection limit is lower.

5. CONCLUSION

This study successfully completed as a partial requirement of nanomaterial master studies program. This thesis presented as courtesy of Solid State Physics Laboratory, Department of Physics and Department of Nanoscience and Nanoengineering, Atatürk University.

Hydrogen is important potential clean energy source. Because renewable, abundant, efficient energy source and provides zero emission (it is the near-future fuel). It is possible that in the future hydrogen will be used more widely as a city gas and to power cars in the same way as natural gas is used. In all these applications some precautions are required for the safe use of hydrogen (H₂) based gas sensor.

Carbon dioxide gas important in global warming, biological and health-related applications-indoor air quality control, process control in fermentation, measurement of CO₂ concentrations in patients' exhaled breath with lung and stomach diseases. In medical applications, it can be critical to monitor the CO₂ and O₂ concentrations in the circulatory systems for patients with lung diseases in the hospital. The current technology for CO₂ measurement typically uses IR instruments, which can be very expensive and bulky. The most common approach for CO₂ detection is based on non-dispersive infrared (NDIR) sensors, which are the simplest of the spectroscopic sensors.

In our study we experimented Indium Tin Oxide In₂O₃:SnO₂ (indium tin oxide or ITO) which is highly degenerate, heavily doped, n-type wide gap semi-conductor (band gap ~3.6-4.2 eV). It having properties such as low electrical resistivity, transparent conducting oxide (TCO). ITO is transparent but bulk form can change color. The current application of ITO films emphasizes the requirement of achieving the lowest possible electrical resistivity with the optimized highest transparency in the visible range. The electrical and optical properties of ITO thin films are critically process

dependent. An optimized performance is sought for an effective application to gas sensor fabrication.

In this study we successfully fabricated simple, robust complementary resistance based Prototype ITO gas sensor device by employing RF magnetron sputtering system, photolithography. These prototype gas sensor devices optimized by different patterns and sizes to enhance surface volume ratio but in our study we tested only three same size and same shape devices. The device fabrication process was unique and could develop in a short time with quality sensing thin film with low cost. We used Al to pattern so electrode easy to etch away when forming patterns on the glass substrate. Deposited thin film characterized by XRD, SEM and Optical absorption techniques which showed interesting results. The procedures we followed to growing ITO thin film was completely experimental and need more studies to conduct to increase its properties in order to have good sensing capabilities. We fabricated five sensor types with different O_2 partial pressure but we discussed here only three types of the sensors. Each sensor type included eighteen (18) different sensors which have different size and pattern. But we discussed only one of size and pattern.

In our study the X-ray diffraction study, SEM images and absorption technique have revealed crystal orientation, grain size, band gap, figure of merit and sensitivity changed relevant to O_2 partial pressure introduced to thin film. All the prepared films show the larger values of transmittance $>90\%$ along with the shift in the fundamental absorption edge and the direct optical band gap which was found to be between 3.46 and 4.13 eV. Absorption measurements show bandgap and figure of merit increasing with increase of O_2 partial pressure. XRD data reveals the dominant peaks as (400) and (441) also while O_2 partial pressure has effects on the intensities and the ratios of these peaks. These devices are sensitive to H_2 and CO_2 concentrations well below 400 sccm at over $50^\circ C$ temperature. Gas-sensing performance was conducted using dynamic gas-sensing system, at elevated temperatures in the range of $30^\circ C$ to $200^\circ C$. The maximum sensitivity ($R_S=22\%$) to H_2 was found at the temperature of $200^\circ C$. CO_2 measurement

shows dependency of the temperature. Response time (92.3 s) and recovery times (24.2 s) are the main features of this device.

In similar kind of study (Yoo *et al.* 2004) explains nano grained ITO thin film gas sensor for H₂ detection nano grain with catalyst 0.5wt% pd and annealed at 650 0C. In our study we have not annealed / post treatment. The changing conditions were Ar:O₂ partial pressure while other parameters constant. The obtained thickness could not maintain for every thin film. Yoo *et al.* (2004) study done using ITO (In₂O₃: SnO₂ =20:80) in our study we used thin film and target ITO (In₂O₃: SnO₂=90:10). They got grain size of SEM images 10-35 nm. Also their thin films was amorphous without anneal while ours thin film having changing crystals according to the partial pressure. Their XRD given 650 - 4h 41.1445 and sensitivity $R_{gas}/R_{air}=0.008$ of 1000ppm.

According to the results concluded in Chapter 4.1 XRD, SEM, Optical Absorption characterization and chapter 4.2. Gas sensor measurement results predict that our thin films and devices having reasonable performance. We could able to achieve fundamental theory of requirement for current application of ITO films emphasizes the requirement of achieving the lowest possible electrical resistivity with the optimized highest transparency in the visible range (Figure of Merit).

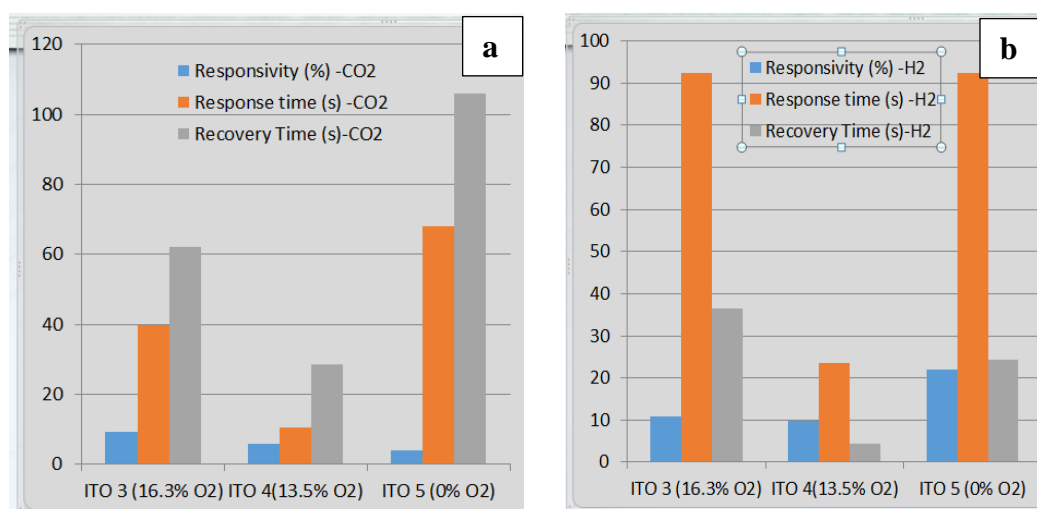


Figure 5.1. Responsivity, Response time, Recovery time for ITO 3, 4, 5 Device at 200°C **a.** CO₂ **b.** H₂

Chart 4.27 shows static representation for H₂ and CO₂ gas responsivity, response time recovery time for ITO 3 (16.3% O₂), ITO 4 (13.3%) and ITO 5 (0% O₂) devices at 200°C. Highest and least response, recovery time should be considered as pair with its percentage. But here include numerical values.

1. Least responsivity shows CO₂ gas for ITO 5 device. (blue color in Chart 4.27.a)
2. Highest responsivity shows H₂ gas for ITO 5 device. (blue color in Chart 4.27.b)
3. Least response time shows CO₂ gas for ITO 4 device. (orange color in Chart 4.27.b)
4. Highest response time shows H₂ gas for ITO 5 device. (orange color in Chart 4.27.b)
5. Least recovery time shows CO₂ gas for ITO 4 device.(gray color in Chart 4.27.b)
6. Highest recovery time shows CO₂ gas for ITO 3 device.(gray color in Chart 4.27.a)
7. Chart 4.27.a shows CO₂ recovery time larger than response time but for H₂ response time greater than recovery time.
8. ITO 5 gas sensor device expected higher figure of merit low bandgap and small grain crystal structure and 400 phase peak.
9. ITO 4 gas sensor device expected higher figure of merit bandgap higher than ITO 5 and poly crystal grain structure and 400 and 441 phase peak.
10. ITO 3 gas sensor device expected higher figure of merit higher bandgap poly crystal structure and 400 and 441 phase peak.

As a conclusion we determined our first and second hypothesis experimentally.

1. Research how the characteristics of the ITO films change when O₂ increase/decrease during the growth?
2. Research how influence Oxygen partial pressure to improve the sensitivity for different gas specious?

5.1. Outlook and Future Work

Required further investigation in this field of study, the following additional experiments will be carried out in future. With regard to sensor properties a further study of the responsivity against reducing and oxidizing gases such as CO₂ and H₂, and other oxidizing gases as well as the stability and reliability of the sensor is needed. The influence of the relative humidity on the response and the selectivity of the sensors at different operation temperatures must be studied. Also same gas sensor need to be experiment forming nanostructured thin film in near future.

REFERENCES

- Ali, M., 2008. Wide band gap materials and devices for NO_x, H₂ and O₂ gas sensing applications. Dissertation zur Erlangung des akademischen Grades Doktor-Ingenieur, vorgelegt der Fakultät Elektrotechnik und Informationstechnik der Technischen Universität Ilmenau, 252p, Ilmenau, Germany.
- Anonim, 2014a. <http://www.grandviewresearch.com/industry-analysis/gas-sensors-market> Browsing date 18.12.2014.
- Ashish Modi, Nikhil Koratkar, Eric Lass, Bingqing Wei, Pulickel M. Ajayan., 2003. Miniaturized gas ionization sensors using carbon nanotubes. *Nature*, 424(6945), 171-174.
- Balaguru, R.J.B., Jeyaprakash, B.G., 2004. Mimic of a Gas sensor, Metal Oxide Gas Sensing Mechanism, Factors Influencing the Sensor Performance and Role of nanomaterials based gas sensors. SASTRA University, Thanjavur, India.
- Barsan, N., Koziej, D., Weimar, U., 2007. Metal oxide-based gas sensor research: How to? *Sensors and Actuators B* 121, 18–35.
- Bel Hadja Tahar, R. Ban, T. Ohar, Y. and Takahashi, Y., 1998. Tin doped indium oxide thin films: Electrical properties. *J. Appl. Phys.* 83(5), 2631-2645.
- Berry, L., Brunet, J., Varenne, C., Mazet, L., Pauly, A., Wierzbowska, K., 2007. NO₂ gas sensing studies : impact of geometrical and physical characteristics of ohmic contacts on n-inp epitaxial sensitive layer. *Materials Science and Engineering: C*, 27(4), 654–658.
- Burstein, E., 1954. Anomalous optical absorption limit in InSb. *Phys. Rev.* 93, 632-633.
- Capone, S., Forleo, A., Francioso, L., Rella, R., Siciliano, P., Spadavecchia, J., Presicce, D.S. and. Taurino, A.M., 2003. Solid state gas sensors: state of the art and future activities. *Journal of Optoelectronics and Advanced Materials*, 5(5), 1335-1348.
- Carl, K.; Schmitt, H.; Friedrich, I., 1997, Optimization of sputtered ITO films with respect to the oxygen partial pressure and substrate temperature, *Thin Solid Films*, 0295(1-2), 151-155.
- Chen, A., Zhu, K., Zhong, H., Shao, Q., & Ge, G., 2014. A new investigation of oxygen flow influence on ITO thin films by magnetron sputtering. *Solar Energy Materials and Solar Cells*, 120, 157-162.
- Chen, Z. Li, W., Li. R., 2013, Fabrication of Highly Transparent and Conductive Indium–Tin Oxide Thin Films with a High Figure of Merit via Solution Processing. *Langmuir*, 29 (45), pp 13836–13842, DOI: 10.1021/la4033282.
- Eggins, B., 2004. *Chemical Sensors & Biosensors*. John Willey & Sons LTD, England, UK, 143p
- Ellmer K., 2000, Magnetron sputtering of transparent conductive zinc oxide: relation between the sputtering parameters and the electronic properties *J. Phys. D: Appl. Phys.*, 33-17.
- Fan, J. C. Bachner, F. J. and Foley, G. H., 1977. Effect of O₂ pressure during deposition on properties of rf-sputtered Sn-doped In₂O₃ films. *Appl. Phys. Lett.* 31, 773-775.

- Fan, J. C. C. and Goodenough, J. B., 1977. X-ray photoemission spectroscopy studies of Sn-doped indium-oxide films. *J. Appl. Phys.* 48, 3524-3531.
- Frank, G. Köstlin, H., 1982. Electrical properties and defect model of tin-doped indium oxide layers. *Appl. Phys.* A27, 197-206.
- Galasso, F. S., 1970. Structure and properties of inorganic solids. Oxford New, York, Toronto, Sydney, Branschweig, Pergamon Press, 90-102.
- Gang, Jian-Wei & Quar-fang Chen, 2005. Developing Miniatur Nano structured Semi Conductor Metal Oxide Gas sensors. *Sensors and Materials*, 18(4).
- Gardon, M., Guilemany, J.M., 2013. A review on fabrication, sensing mechanisms and performance of metal oxide gas sensors. *J Mater Sci: Mater Electron*, 24, 1410–1421.
- Gu, H., Wang, Z. and Hu, Y., 2012. Hydrogen Gas Sensors Based on Semiconductor Oxide Nanostructures. *Sensors*, 12, 5517-5550.
- Hamberg, H. Granqvist, C. G., 1989. Evaporated Sn-doped In₂O₃ films: Basic optical properties and applications to energy-efficient windows. *J. Appl. Phys.* 60(11), 123-159
- Hagen, W., Rainer E. Lambrich, Logois, J., 1983. Semiconducting gas sensors. *Advances in Solid State Physics Volume 23*, pp 259-274.
- Horsfall, A. and Wright, N., 2006. Sensing the extreme, physicsweb.org. <http://www.ncl.ac.uk/eee/assets/news-files/PWMAY06horsfall.pdf> (23.12.2014).
- Jiao, Z., Wu, M., Gu, J., Sun, X., 2003. The gas sensing characteristics of ITO thin film prepared by sol-gel method. *Sensors and Actuators B*, 94, 216–221.
- Kanan, S.M., El-Kadri, O.M., Abu-Yousef, I.A. and Kanan, M.C., 2009. Semiconducting Metal Oxide Based Sensors for Selective Gas Pollutant Detection. *Sensors*, 9, 8158- 8196.
- Kang, B.S., Wang, H.T., Tien, L.C., Ren, F., Gila, B.P., David P., Kosiorek, A., Kandulski, W., Glaczynska, H. and Giersig, M., 2005. Fabrication of Nanoscale, Rings, Dots, and Rods by Combining Shadow Nanosphere Lithography and Annealed Polystyrene Nanosphere Masks. *small*, 1 (4), 439–444.
- Kerkache, L., Layadi, A., Hadjersi, F., Dogheche, E., Gokarna, A., Stolz, A., Halbwax, M., Vilcot, J.P., Decoster, D., El Zein, B., Habib., S.S., 2010. Sputtered Indium Tin Oxide thin films deposited on glass substrate for photovoltaic application. *International Conference on Renewable Energies and Power Quality (ICREPQ'10) Granada, Spain*.
- Kim, J. H., Lee, J. H., Heo, Y. W., Kim, J. J., & Park, J. O., 2009. Effects of oxygen partial pressure on the preferential orientation and surface morphology of ITO films grown by RF magnetron sputtering. *Journal of electroceramics*, 23(2-4), 169-174
- Kim, S., Choi, J., Jung, M., Joo, S. and Kim, S., 2013. Silicon Carbide-Based Hydrogen Gas Sensors for High-Temperature Applications. *Sensors*, 13, 13575-13583.
- Klabunde, K., 1986. Thin films from free atoms and particles. 376p, University of Michigan, USA, Elsevier.
- Kukkola, J., 2013. Gas sensors based on nanostructured tungsten oxides. Phd thesis, University of Oulu, Finland
- Kulkarni, A. K. and Knickerbocker, S. A., 1996. Estimation and verification of the electrical properties of indium tin oxide based on the energy band diagram. *J. Vac. Sci. Technol. A* 14(3), 1709-1713.

- Kurdesau, F., Khripunov, G., Da Cunha, A. F., Kaelin, M., & Tiwari, A. N., 2006. Comparative study of ITO layers deposited by DC and RF magnetron sputtering at room temperature. *Journal of non-crystalline solids*, 352(9), 1466-1470.
- Letter to the editor, Nature of an ohmic metal-semiconductor contact, 1960 *Physica* 26889
- Lupan a,b, Guangyu C., Lee C., 2008. Novel hydrogen gas sensor based on single ZnO nanorod. *Microelectronic Engineering* 85, 2220–2225
- M. Batzill, U. Diebold, 2005. The surface and materials science of tin oxide/*Progress in Surface Science*, 79, 47–154.
- MacGrath, Michael J. & Clodhana N. S., 2013. *Sensor Technologies*, Intel Labs, 336p, Europe.
- Michael A., Lang O., Brubakk., 2008. *The Future of Diving*. Smithsonian institution scholarly press, 13(978), 9788460.
- Michal, A. Carpentor, Sanjay Mathur, Andrei Kolmatov, 2013. *Metal oxide nano materials for Chemical Sensors*. Springer.
- Mohd H.Y., 2012. *Investigation of Metal Oxide Nanostructured Thin Films Based Optical Hydrogen Sensors*. Phd thesis, University Melbourne, Australia.
- Moss, T. S., 1954. The interpretation of the properties of indium antimonide. *Proc. Phys. Soc. London, Sect. B*67, 775-782.
- Nadaud, N. Lequeux, N. Nanot, M. Jové, J. and Roisnel, T., 1998. Structural studies of tin-doped indium oxide (ITO) and In₄Sn₃O₁₂. *J. Solid State Chem.* 135, 140-148.
- Norton, D.P., Abernathy, C.R., Lin, J. and Pearton, S.J., 2006. Wide Bandgap Semiconductor Nanorod and Thin Film Gas Sensors. *Sensors*, 6, 643-666.
- Paul K. Chu, Chapter 5, City University Hong, 2005. <http://www.cleanairtechnology.com/cleanroom-classifications-class.php>
- Pearton, S.J., Ren, F., Wang, Y.L., Chu, B.H., Chen, K.H., Chang, C.Y., Lim, W., Lin, J., Norton, D.P., 2010. Recent advances in wide bandgap semiconductor biological and gas sensors. *Progress in Materials Science* 55, 1–59.
- Perkowitz S., 1993. *Optical Characterization of semiconductors: Infrared, Raman, and Photoluminescence Spectroscopy*. Academic press Limited, 38p, CA, USA.
- Qiao aus Hebei, 2003. *Fabrication And Study Of ITO Thin Films Prepared By Magnetron Sputtering*. PhD thesis, University of Duisburg-Essen, Essen, Germany.
- Rajnikant, A., Shukla, S., Ludwig, L., Anjum, M., Cho, H.J. and Seal, S., 2004. A Nanoparticle-based Microsensor for Room Temperature Hydrogen Detection. *IEEE*. 395-398.
- Schroder D. K., 2006. *Semiconductor Materials and Device Characterization*, 3rd Edition, John Wiley & Sons, Inc. NJ, USA.
- Schwartz, G.C, Srikrishnan, K.V., 2006. *Handbook of Semiconductor Interconnection technology*, 2nd edition. CRC press, Taiter & Francis Group LLC, FL, USA.
- Terzini, E., Thilakan, P., Minarini, C., 200. Properties of ITO thin films deposited by RF magnetron sputtering at elevated substrate temperature. *Materials Science and Engineering B*77, 110–114.
- Wang, C. and et al, 2010. Metal Oxide Gas Sensors: Sensitivity and Influencing Factors. *Sensors*, 10, 2088-2106.

- Webster, J.G., 1999. *The Measurement, Instrumentation and Sensors Handbook*, CRC/IEEE Press, Boca Raton, FL.
- Weiher, R. L. and Ley, R. P., 1966. Optical properties of indium oxide. *J. Appl. Phys.* 37(1), 299-302.
- Weijtens, C. H. L., 1990. Indium tin oxide for solid-state image sensors. PhD Thesis, Eindhoven University of Technology, North Brabant, Netherlands.
- Wright, J.S., Lim, W., Norton, D.P., Pearton, S.J, Ren, F., Johnson, J.L., and Ural, A., 2010. Nitride and oxide semiconductor nanostructured hydrogen gas sensors. *Semicond. Sci. Technol.* 25, 024002.
- Yamada, N. Yasui, I. Shigesato, Y. Li, Y. Ujihira, Y. and Nomura, K., 1999. Doping Mechanisms of Sn in In₂O₃ Powder Studied Using ¹¹⁹Sn Mössbauer Spectroscopy and X-Ray Diffraction. *Jpn. J. Appl. Phys.* 38(5A), 2856-2862.
- Yamazoe, N., 2005. Toward innovations of gas sensor technology, *Sensors and Actuators B* 108, 2–14
- Yamazoe, N., 2005. Toward innovations of gas sensor technology. *Sensors and Actuators B* 108, 2–14.
- Yamazoe, N., Sakai, G. and Shimano, K., 2003. Oxide semiconductor gas sensors. *Catalysis Surveys from Asia* 7 (1), 63-75.
- Yang T., 2007. Capacitance-Voltage studies of atomic-layer-deposited mos structures on gallium arsenide and other iii-v compound semiconductors. MS thesis. Purdue University, west Lafayette, India.
- Yoo, K.S.Y., Park, S.H., Kang, J.H. 2005. Nano-grained thin-film indium tin oxide gas sensors for H₂ detection. *Sensors and Actuators B* 108, 159–164.
- Zhang, J, Hu, P., Zhang, R., Wang, X., Yang, B., Cao, W., Li, Y., He, X., Wang, Z. and O'Neill, W., 2012. Soft-lithographic processed soluble micropatterns of reduced graphene oxide for wafer-scale thin film transistors and gas sensors. *J. Mater. Chem.* 22, 714.

RESUME

Sri Lankan born Sadna IŐIK migrated to Turkey in 2003. She started her undergraduate studies in Computer Engineering at Fatih University, Istanbul and graduated in 2011; later started her master studies in Nanomaterial at Atatürk University, Erzurum in 2013. Sadna continues her carrier as a Computer Engineer. She has a fluent command of English and Turkish languages.